The Dissertation Committee for Eric Joseph Guiltinan Certifies that this is the approved version of the following Dissertation:

Multiphase Flow Properties of Sealing Caprocks for CO_2 Geological Storage

Committee:

Meinhard Bayani Cardenas, Supervisor

David Nicolas Espinoza, Co-Supervisor

Philip C. Bennett

Charlie J. Werth

Peter B. Flemings

Multiphase Flow Properties of Sealing Caprocks for CO_2 Geological Storage

by

Eric Joseph Guiltinan

Dissertation

Presented to the Faculty of the Graduate School of

The University of Texas at Austin

in Partial Fulfillment

of the Requirements

for the Degree of

Doctor of Philosophy

The University of Texas at Austin

August 2018

Acknowledgements

Abstract

Multiphase Flow Properties of Sealing Caprocks for CO₂ Geological Storage

Eric Joseph Guiltinan, Ph.D.

The University of Texas at Austin, 2018

Supervisor: Meinhard Bayani Cardenas

Co-Supervisor: David Nicolas Espinoza

At the pore-scale, intermolecular forces are responsible for wetting, solubility, phase separation, and interfacial tension. These forces along with the pore structure, in porous media, and aperture distributions, in fractures, govern the physics of multiphase fluid flow and result in continuum scale parameters such as residual saturation and relative permeability. However, these forces are often overlooked and poorly understood. In this dissertation we explore how the pore-scale contributes to multiphase flow with an emphasis on geologic CO₂ sequestration and caprock integrity. First, we explore the wettability of organic shales, a likely caprock, for CO₂ storage. We provide the first reservoir condition brine/supercritical CO₂ contact angle measurements on an organic shale and find the organic shale to be water wet with little effect of organic content and thermal maturity. This means that capillary forces can hold back large CO₂ columns in these caprocks. Second, we investigate how pore structure controls the breakthrough pressure of mudstones through the use of resedimentation experiments combined with mercury intrusion porosimetry. We offer novel insights into the relationship between the coarse grained

percolating network and the fine grained void ratio and show that the breakthrough pressure is related to the fine grained void ratio through a power-law. Third, we incorporate intermolecular forces into a numerical model to explore how heterogeneous wetting distributions contribute to the flow of CO_2 in fractures. We discover that the heterogeneous wetting contributes to residual saturation in fractures by providing opportunities for the predominately non-wetting CO_2 to surround the wetting phase. The wetting distribution also contributes to breakthrough time and the evolution of unsteady relative permeability. These results provide fundamental insight into how pore scale forces control continuum scale multiphase flow.

Table of Contents

List of Tables

List of Figures

Chapter 1: Introduction

1.1 A CASE FOR CARBON CAPTURE AND STORAGE

Rising atmospheric greenhouse gas concentrations are causing the Earth to warm at a rate that is unprecedented in the last millennia [*Edenhofer et al.*, 2014]. This is being driven by a striking rise in global CO_2 emissions (Figure 1.1).
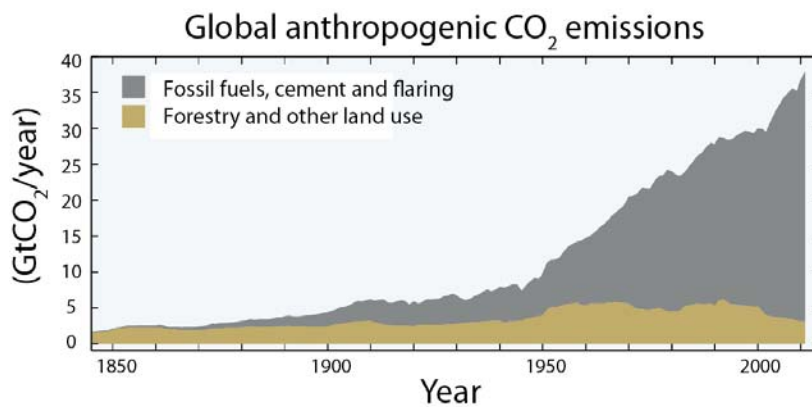
Figure 1.1: Global anthropogenic CO_2 emissions from forestry and other land use as well as from burning of fossil fuel, cement production and flaring. Modified from [*Edenhofer et al.*, 2014].

The nearly exponential growth in emissions is mostly due to the rapid industrialization of countries within the organization for economic co-operation and development (OECD). Recently OECD population growth has slowed and energy efficiencies have stabilized the energy demands from these countries; however, the population growth and industrialization of non-OECD countries is forecast to continue. In fact, the U.S. Energy Information Administration (EIA) forecasts global energy consumption to grow by 28% between 2015 and 2040 [*EIA*, 2017] (Figure 1.2).

1
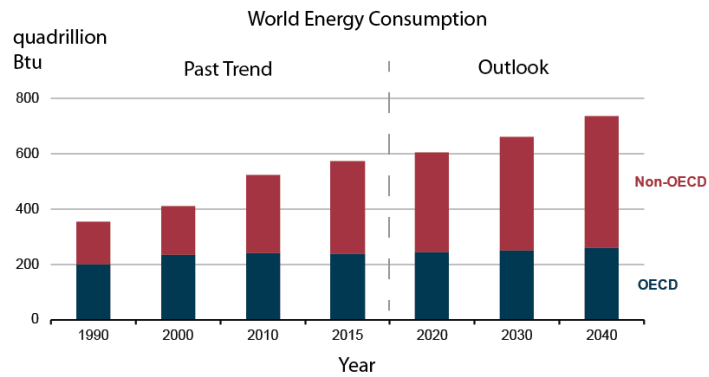
Figure 1.2: U.S. Energy Information Administration, world energy consumption past and forecasted future. Modified from [*EIA*, 2017]

Many hope that the adoption of renewable energies such as wind and solar can cause a reduction in the global emissions of CO_2, unfortunately, this seems unlikely given the burdensome pace of increasing energy demand. Even considering a dramatic rise in the adoption of renewables we are likely to remain dependent on fossil fuels for the considerable future (Figure 1.3).
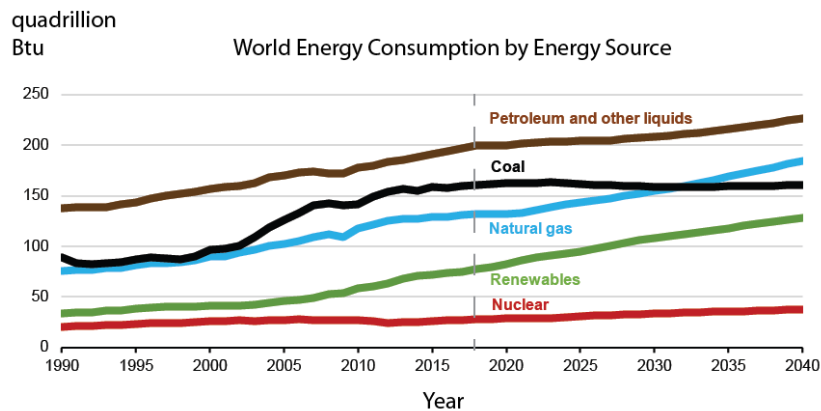
Figure 1.3: U.S. Energy Information Administration. World energy consumption by source, past and forecasted future [*EIA*, 2017].

Today the largest source of energy comes from liquid hydrocarbons which are used predominately in transportation. The EIA forecasts this to continue, but the widespread adoption of electric vehicles has the potential to change this. Britain, France, India, Norway, and the Netherlands have all announced dates to ban the sale of gasoline and diesel vehicles and other countries have announced their intentions of following [*Petroff*, 2017]. While electric vehicle sales make up only a small fraction of total vehicles sales they are being adopted at a rapid pace (Figure 1.4) [*IEA*, 2017]. The shift to electric vehicles will transfer the energy demand from liquid hydrocarbons to the electric grid. If true, this scenario would require additional electrical capacity and present a significant opportunity for reducing CO_2 emissions by utilizing carbon capture and storage (CCS) at new power plants.
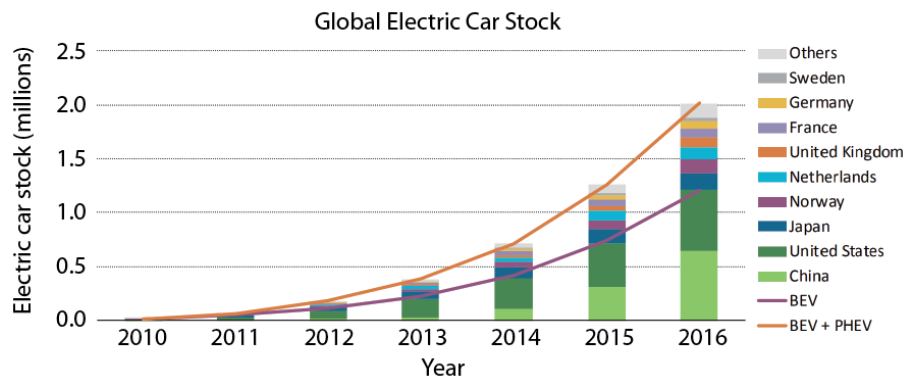
Figure 1.4: International Energy Agency (IEA), global electric car stock. The purple line represents the total battery electric vehicles and the purple line represents both plug in hybrids and batter only vehicles [*IEA*, 2017].

CCS is the processes by which CO_2 is removed from large point sources such as power plants and cement manufactures. Once removed the CO_2 can be disposed of in deep geologic formations where it is permanently trapped. It is estimated that saline aquifers

have the capacity for 1,000 to 10,000 Gton of CO_2 [*IPCC*, 2005]. The lack of widespread adoption of CCS is likely due to the financial burden of capture. The cost for onshore storage of CO_2 in the USA is estimated to be less than \$5/tCO_2 [*Benson et al.*, 2005], but the cost of capture is much higher. In a comprehensive study, *Rubin et al.* [2015], estimate that capture at coal-based integrated gasification combined cycle power plants ranges from \$38 to \$84/tCO_2 and natural gas combined cycle plants range from \$59 to \$143/tCO_2. Norway, with a tax of approximately \$50/tCO_2 emitted to the atmosphere, is the only country in Europe conducting CCS with three projects that strip nearly 2 million tons of CO_2 from natural gas each year. Last year in Houston, Petra Nova, the first predominately privately funded CCS project began to strip CO_2 from the flue gas of a coal power plant and use it for enhanced oil recovery (EOR). Selling captured CO_2 for EOR and the existence of a CO_2 pipeline for distribution to the large oil and gas sector makes Texas an ideal place for CCS.

Two very recent developments provide hope that the economics of CCS are changing. First, the US Federal Bipartisan Budget Act of 2018 provides a \$50/ton credit to any firm that sequesters CO_2 that was otherwise going to be emitted to the atmosphere. In addition they can receive \$35/ton if they sell CO_2 to an oil company for EOR. This credit will provide the same function as Norway's tax; it places a significant price on CO_2 emissions. The second recent development is the construction of the NET Power power plant in Houston. This novel power plant uses supercritical CO_2 as its working fluid. Natural gas is burned directly into a stream of supercritical CO_2 which is used to power turbines and generate electricity. Known as the "Allam Cycle", this process allows for 100% of the emissions to be collected and electricity to be produced at a similar price to conventional natural gas combined cycle plants [*Allam et al.*, 2017]. The 50 megawatt pilot plant is currently in the start up phase with larger full scale plants in the planning

stages. NET Power's success is not guaranteed, but this project demonstrates the possibility that a technologically breakthrough on the capture side could have dramatic implications for CCS. The new tax credit will mean tens to hundreds of millions of dollars per year in revenue to NET Power and Petra Nova, two projects which were already economically viable, and could mean the beginning of many more CCS projects.

1.2 MOTIVATION

The NET Power plant proposes to operate at high temperature and pressure. At these conditions the CO_2 is a supercritical fluid that is much more dense than at ambient conditions and has properties of both a liquid and gas. These properties help drive turbines to efficiently generate electricity. The same conditions exist in deep reservoirs and allow for the storage of large volumes of CO_2. However, reservoir conditions make conducting and observing experiments difficult. One way researchers get around this is by using fluid pairs that have the same viscosity ratios. These experiments can capture the viscous behavior of scCO2 and brine but they miss the intermolecular forces which control fluids at the pore-scale.

At the pore-scale the fluid-fluid properties and fluid-solid properties control the wettability and interfacial tension of the brine/scCO2/reservoir system. Wettability and interfacial tension, in turn, control continuum scale properties such as residual saturation and permeability [*Chaudhary et al.*, 2013; *Juanes et al.*, 2006]. These forces are temperature and pressure dependent [*Stefan Iglauer et al.*, 2015] and therefore conducting experiments at reservoir conditions is important for understanding the multiphase system.

Pore-scale multiphase fluid flow is governed by the Young-Laplace equation [*Laplace et al.*, 1829; *Young*, 1805]:

$$P_c = \frac{2\sigma \cos(\theta)}{r} \tag{1.1}$$

5

where θ is the contact angle of formation brine in the presence of supercritical CO_2 (scCO2), σ is the interfacial tension between the brine and scCO2, r is pore radius, and P_c is the capillary pressure, or the pressure required for a nonwetting phase to displace a wetting phase within the pore. The contact angle is the angle produced by the interface within a pore and it describes the wettability of the system. The influence of wettability on multiphase fluid flow is well known, however what controls the contact angle is not. Numerous studies on quartz, an analog for sandstone, and mica, an analog for clay, have produced contact angles which range from 0° to 92° [*Stefan Iglauer et al.*, 2015]. The reason for the discrepancy is likely due to organic molecules which adsorb to the surface of the quartz [*S. Iglauer et al.*, 2014]. Understanding the contact angle of laboratory cleaned samples is important for a fundamental understanding of what controls the contact angle; however, if laboratory samples are readily contaminated by airborne organic molecules than applying these measurements to reservoirs that have been exposed to geologic fluids over geologic time-scales is questionable.

The Young-Laplace equation can be used to predict the entry pressure of scCO2 into a caprock by estimating the contact angle and the maximum pore throat. The entry pressure is important because once scCO2 begins to enter the caprock the surface area for chemical reactions is increased and chemical weathering may deteriorate the integrity of the caprock [*Ilgen et al.*, 2017]. While understanding the entry pressure is important, flow through the caprock is not initiated until the breakthrough pressure has been reached. The breakthrough pressure is important from a CCS perspective because it can be used to predict the total column height of CO_2 which can be securely stored. It is also important from an oil exploration stand point because it predicts the maximum expected hydrocarbon reserves. The breakthrough pressure is theoretically the capillary pressure at the smallest pore throat of an interconnected pathway of pores across a sample. This pore throat is

difficult to predict without conducting experiments. A variety of scCO$_2$ breakthrough pressure experiments have been conducted on caprocks with varied results [*Harrington et al.*, 2009; *Hildenbrand et al.*, 2002; *Hildenbrand et al.*, 2004; *Wollenweber et al.*, 2010]. These experiments are time consuming and difficult to conduct. Estimating breakthrough pressure from properties such as porosity, void ratio, or mineralogical content would be helpful for quickly evaluating caprock integrity for CCS and for estimating hydrocarbon reserves.

Finally, fractures within caprocks offer high permeability conduits to the surface and are important for the flow of fluids in natural process, engineering uses, and in evaluating CO$_2$ sequestration security. Multiphase flow in fractures is controlled by the fracture geometry, fluid properties, wettability, and the pressure gradients. Due to the difficulty in incorporating pore-scale intermolecular forces in conventional fluid dynamic models the wettability of fractures has been relatively unexplored. However, these forces have the potential to have large impacts on the CO$_2$ flow behavior, including on the evolution of relative permeability, the breakthrough time, and the residual saturation of scCO$_2$.

1.3 RESEARCH QUESTIONS

In this dissertation I seek to explore how the pore-scale influences the core-scale to continuum scale with an emphasis on caprock seal integrity during CCS. In the proceeding chapters I present the results of novel research conducted during my PhD. First, I present the first scCO$_2$ experiments on an organic shale in order to understand how this common caprock may withstand buoyant forces. Second, I seek to identify the controls on breakthrough pressure through exploring synthetic mudrocks with controlled mineralogies and grain size distributions. And third, I apply the numerical method known as the lattice

Boltzmann method, to explore how the intermolecular forces responsible wetting control the evolution of residual saturation and permeability during a scCO$_2$ flood.

Specifically, this research seeks to answer the following questions:

1. *What is the wettability of scCO$_2$ and brine on shales?*

2. *What is the influence of organic matter concentration, thermal maturity, temperature,   and pressure on the wettability of shales?*

3. *Does the mineralogy of caprocks influence their breakthrough pressure?*

4. *Can we predict the breakthrough pressure based upon the grain size distribution?*

5. *Do the intermolecular forces responsible for wetting affect the flow of scCO$_2$ in fractures?*

6. *Do heterogeneous wetting distributions effect the evolution of permeability and residual saturation during multiphase flow in fractures?*

1.4 DISSERTATION OUTLINE

The main findings of this research are presented in chapters two, three, and four with a summary of the findings and suggested future research included in Chapter five. Each main chapter was written with publication in a scholarly journal in mind and thus contains its own introduction, methods, results, discussion, and conclusion sections; however, the references have been compiled at the end of the dissertation. Chapter 2 has been published in the International Journal for Greenhouse Gas Control, Chapter 3 is undergoing revisions before resubmittal, and Chapter 4 will be submitted for publication shortly.

Chapter 2: The effect of organic matter and thermal maturity on the wettability of supercritical CO_2 on organic shales

2.1 ABSTRACT

The geologic sequestration of CO_2 is a potential solution for decreasing anthropogenic atmospheric CO_2 emissions by trapping it underground. A primary mechanism for storage is structural trapping where low permeability and high capillary entry pressure caprock materials hold back the buoyant CO_2 from rising to the surface. The wettability (or contact angle) of reservoir and caprock materials in relation to CO_2 and formation brine partly determines the efficiency of structural trapping. Current practice applies the results of individual reservoir-comprising minerals recorded under laboratory conditions, to rocks under in-situ reservoir conditions. However, the wide variety of measured contact angles reported in the literature calls this practice into question. Moreover, organic shales have not been the focus of systematic studies. Here we analyzed the wettability of CO_2 on organic shales at various organic matter concentrations and thermal maturities. We found that bulk organic shale remains highly water wet with respect to CO_2 despite changes to the maturity or concentration of organics. This finding is in contrast to recent molecular dynamic simulations and our initial expectations from previous pore-scale analyses in which organic matter was shown to be hydrophobic. The results are likely due to the remaining mineralogy of the rock dominating the wetting behavior despite concentrations of organics up to 7.9%. This means that reservoirs and aquifers capped by organic rich caprocks may be suitable locations for CO_2 storage and that organic matter at concentrations below percolation threshold may not have a detrimental effect on structural trapping efficiency.

2.2 INTRODUCTION

2.2.1 Wettability and Structural Trapping

The sequestration of anthropogenic carbon dioxide (CO_2) in deep geologic formations has been proposed as a method to mitigate further increases in the concentration of atmospheric CO_2. One of many demonstration projects around the world is the "Sleipner project" in the North Sea where one million tons of CO_2 have been injected each year. Recent work on the Sleipner project has revealed the buoyant migration of CO_2 through multiple shale beds due to "unexpectedly low threshold [capillary] pressures for vertical migration" [Cavanagh and Haszeldine, 2014]. While the authors conclude these lower threshold pressures are due to micro fractures the wettability of the shale beds should not be disregarded.

The capillary entry pressure (P_c) for buoyant CO_2 to rise through a caprock is controlled by the wettability of the brine, supercritical CO_2 (scCO_2), and reservoir rock system (brine/scCO_2/rock). The relationship between the contact angle (Θ) and the capillary entry pressure is described by the Young-Laplace Equation [Laplace et al., 1829; Young, 1805]

$$P_c = \frac{2\sigma \cos(\theta)}{r} \qquad (2.1)$$

where σ is the interfacial tension between the two fluids and r is the radius of the capillary. The primary sealing mechanism of a caprock, commonly called "structural trapping", is therefore related to the wettability of the brine/scCO_2/caprock system and the radius of the largest connected pore throat. The pressure generated due to the buoyancy of a continuous CO_2 column trapped beneath a caprock is:

10

$$P_b = (\rho_b - \rho_g)gh \qquad\qquad (2.2)$$

where ρb is the brine density, ρg is the CO_2 density, g is the gravitational acceleration, and h is the height or thickness of the CO_2 plume. By equating P_b and P_c we can find the height of a CO_2 plume which can be stored beneath a caprock before CO_2 invasion will occur, so that:

$$h = \frac{2\sigma \cos(\theta)}{(\rho_b - \rho_g)gr} \qquad\qquad (2.3)$$

The average radius of a shale pore can vary from 5 of nanometers to 100s of nanometers [Nelson, 2009]. Assuming shale is water-wet ($\theta < 90°$), these small pores retain buoyant CO_2 directly proportional to P_c; however, if shale is CO_2-wet ($\theta > 90°$), then P_c is negative and the rock may spontaneously imbibe CO_2. A negative P_c is equivalent to a suction force, which would pull CO_2 into the shale caprock.

The breakthrough pressure of a given shale can be calculated using (Eqn 2.1) with the minimum pore throat radius, r^*, along an interconnected and continuous path of pores across the shale unit. This r^* is usually larger than the mean r and can be related to the mean pore size and the standard deviation of the pore size distribution [Espinoza and Santamarina, 2010]. Hildebrand et al. [2004], conducted CO_2 breakthrough tests on a series of mudstones, sandstones and other sedimentary rocks by applying a pressure gradient assumed to be greater than the breakthrough pressure and then monitoring the pressure drop as flow occurred across the sample. The pressure at which flow ceased is therefore the breakthrough pressure and was found to fall between 0.1 and 4.9 MPa. Harrington et al. [2009] conducted step-wise increasing pressure experiments with nitrogen

on the Sleipner caprock and found the initial breakthrough pressure to be 3.1 MPa. However, after flow was achieved the pressure dropped to 1.6 – 1.9 MPa. Skurtveit et al., (2012) conducted similar experiments but with CO_2 and found breakthrough pressure on a North Sea shale to range from 3.5 to 4.3 MPa.

From percolation theory the percolation threshold is the minimum porosity at which a connected pathway across a porous medium will form. If we assume that organic matter is CO_2-wet then we can consider the distribution of organic matter in a shale as the pores in percolation theory. In this context, the percolation threshold is the minimum concentration of organic matter which would create a connected path of organic matter pores across a shale layer. Percolation theory predicts that in a randomly distributed porous medium this threshold is met at approximately 12% [Larson et al., 1980]. However, the laminated nature of organic matter in shales, like the Barnett, mean the percolation threshold may be lower in the direction of the laminations and higher across the laminations. This is confirmed by percolation theory in anisotropic materials [Lucena et al., 2003; Masihi et al., 2006; Sadeghnejad et al., 2010].

In addition, shales are often fractured and the fracture openings can effectively behave as larger pore-throats at a large scale. The ability for these fractures to transmit CO_2 through a caprock is, therefore, partially controlled by the wettability of the rock. A second barrier to contain buoyant CO_2 is the effect of friction and viscous forces which can be quantified in terms of rock permeability, relative permeability to CO_2, caprock thickness and the corresponding total head gradient [Downey, 1984; Espinoza, 2011].

2.2.2 Recent Wettability Studies

Until recently, our understanding of the wettability of shale with respect to $scCO_2$ and brine was limited to studies on analogous minerals. Mica, a clay mineral and a

component of clay sediment, is typically used to represent shale. Mica has a large flat crystal structure which makes it well suited for wettability studies [Iglauer et al., 2015a]. Yet, there is little agreement in contact angle measurements of $scCO_2$ and brine on mica [Broseta et al., 2012; Chiquet et al., 2007; Farokhpoor et al., 2013; Mills et al., 2011; Wang et al., 2013]. Additionally, studies on quartz, an analog for tectosilicates, are also inconclusive with contact angles reported in the literature varying between 7° and 92° [Bikkina, 2011; Espinoza and Santamarina, 2010; Farokhpoor et al., 2013; Jung and Wan, 2012; Mills et al., 2011; Wang et al., 2013]. Contamination and differing sample preparation during previous wetting experiments is likely the cause of the disagreement in the literature on the contact angle for quartz and mica [Iglauer et al., 2014]. Given the uncertainty in contact angle measurements and the fact that clays and shales have been shown to become mixed-wet when exposed to crude oil [Borysenko et al., 2009], the need to understand the wetting of shale caprocks is important for CO_2 geological storage. An alternative approach is to measure directly capillary pressure on rock samples [Tokunaga et al., 2013]. If conditions exist at which shale becomes CO_2-wet, then these rocks may facilitate the migration of CO_2 out of the reservoir and into overlying aquifers or escape back into the atmosphere.

Recent investigations into the wettability of a non-organic shale/$scCO_2$/brine system found shale to be water-wet, as expected [Shojai Kaveh et al., 2016]. The authors determined that there is a "low possibility of capillary breakthrough of CO_2 from silty shale caprocks". Iglauer et al. [2015b] also investigated the effect of pressure on the wetting of a non-organic shale/$scCO_2$/brine system but found that it approached mixed wet at higher pressures. Two individual shale wetting results have been reported on an organic shale and showed $scCO_2$ to be water-wet (but approaching mixed wet) with a contact angle of 62° and 59° at 0.1 MPa-25°C and 22.8 MPa-71°C, respectively [Chaudhary et al., 2015].

Recent molecular dynamic simulations indicate that oil wetting on organic matter may increase as a function of thermal maturity with organic material becoming oil-wet as maturity increases [Hu et al., 2016]. It has also been shown that organic shale may be oil-wet when exposed to hydrocarbons [Lan et al., 2015]. These results are concerning because CO_2 storage projects may use an organic shale as a caprock. Also, depleted oil and gas reservoirs are promising locations due to their proven ability to trap hydrocarbons and the presence of necessary infrastructure for CO_2 transport and injection. CO_2 spontaneous imbibition in shales may be detrimental to capillary entry pressure of organic shale caprocks, such as, the Longyearbyen CO_2 storage project in Svalbard, Norway [Bohloli et al., 2014], and the SACROC Nothern Platform (Hans, 2010). On the other hand, spontaneous imbibition of CO_2 in organic pores could be advantageous to CO_2 sequestration in the pore space of shales themselves through capillary trapping and sorption mechanisms [Busch et al., 2016].

In this paper we investigate the effect of total organic carbon (TOC) as well as organic thermal maturity, represented by vitrinite reflectance (Ro), on the contact angle of a brine/scCO$_2$/shale system. We first introduce the samples selected and their preparation. Next, we discuss the recently developed methodology for determining contact angles in opaque capillaries and briefly describe the algorithm used to measure the contact angles. Finally, we present our results, compare our results to previous measurements in the literature, and discuss the implications for CO_2 storage. The over-all goal of this work is to evaluate the potential of structural CO_2 trapping capacity in geological formations capped by an organic-rich shale caprock.

2.3 METHODS

2.3.1 Shale Samples

To investigate the wetting of CO_2 on organic shales we used samples from the Barnett Shale. The Barnett Shale is a siliceous organic shale composed primarily of clay to silt-size quartz, illite, and, carbonate, with a minor amount of smectite type clays, pyrite, and phosphates [Loucks and Ruppel, 2007]. Vitrinite reflectance values generally increase with depth; however the highest Ro values are found in the west where the formation was heated by Tertiary aged intrusives [Kinley et al., 2008]. The organic content is highest in the clay rich intervals of the Barnett and typically ranges from 3 and 13% [Montgomery et al., 2005]. The kerogen in the Barnett is a marine Type II kerogen with 95-100% amorphous organic matter [Jarvie et al., 2007].

Seven organic shale samples from five different wells in the Barnett Shale were acquired. This sample suite contains a wide range of thermal maturity (0.58 – 2.07 % Ro) and TOC (3.27 – 7.88 %). Ro values were calculated according to the formula suggested by [Jarvie et al., 2007] and using Tmax, the temperature at which the maximum release of hydrocarbons occurs during pyrolysis, as reported in Zhang et al. [2014]. Methane sorption experiments were conducted on some of these samples and sorption was found to be a function of TOC [Zhang et al., 2012], suggesting that organic matter plays an important role in surface phenomena-dependent processes. Mineralogical data was acquired from XRF analysis. The locations of the wells where the samples were collected are shown in Figure 2.1 and the mineralogical data is presented in Table 2.1.

15
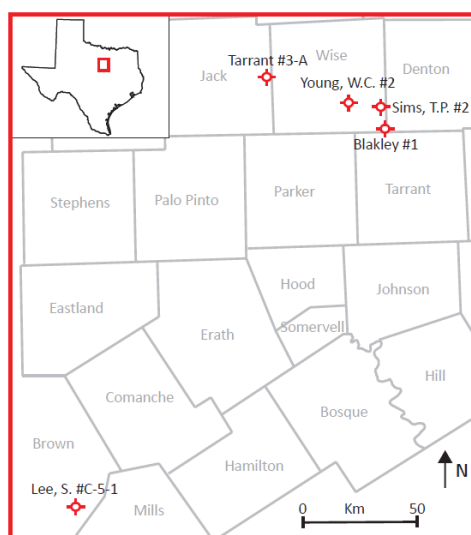
Figure 2.1: Well location map where shale samples were sourced from (modified from [Zhang et al., 2014]). The red square in the inset map of the state of Texas, USA shows the general location of the large map . The wells are denoted by crossed, red circles with corresponding names. The gray text and borders denote county limits.

Well	Depth (meters)	R_o (%)	TOC (mass %)	Mineralogy (mass %)					
				Kaolinite	Illite	Quartz	Calcite	Dolomite	Others
Sims, T.P. #2	2359.8	2.02	6	18.9	43.8	19.8	0.0	2.7	14.8
Sims, T.P. #2	2326.8	1.6	3.6	13.4	31.1	37.9	0.1	1.1	16.3
Young, W.C. #2	2108.6	1.23	4.5	14.4	33.4	37.6	1.8	0.5	12.2
Tarrant #3-A	1878.8	0.81	7.1	13.7	31.9	26.7	4.2	0.2	23.4
Tarrant #3-A	1880.0	1.03	3.3	11.1	25.9	16.3	11.8	0.0	34.9
Lee,S. #C-5-1	381.0	0.58	7.9	12	27.8	34.7	3.6	2.2	19.7
Blakely #1	2201.6	2.16	4.1	2.2	5.1	33	22.9	2.8	34

Table 2.1: Mineralogical data for shale samples analyzed. Well locations are shown in Figure 2.1. Ro is vitrinite reflectance and TOC is short for total organic carbon. The well locations are shown in Figure 2.1.

16

2.3.2 Sample Preparation

The samples were prepared by drilling a 1.5 mm-diameter capillary perpendicular to bedding using a high-speed precision drill press (Cameron Micro Drill Press, model# 214) cooled with water. This drill press operates at 30,000 rpm ensuring the smoothest possible surface we could achieve. The capillary was extended only partially through the sample so as to create a "basket" for the brine to sit in (Figure 2.2).
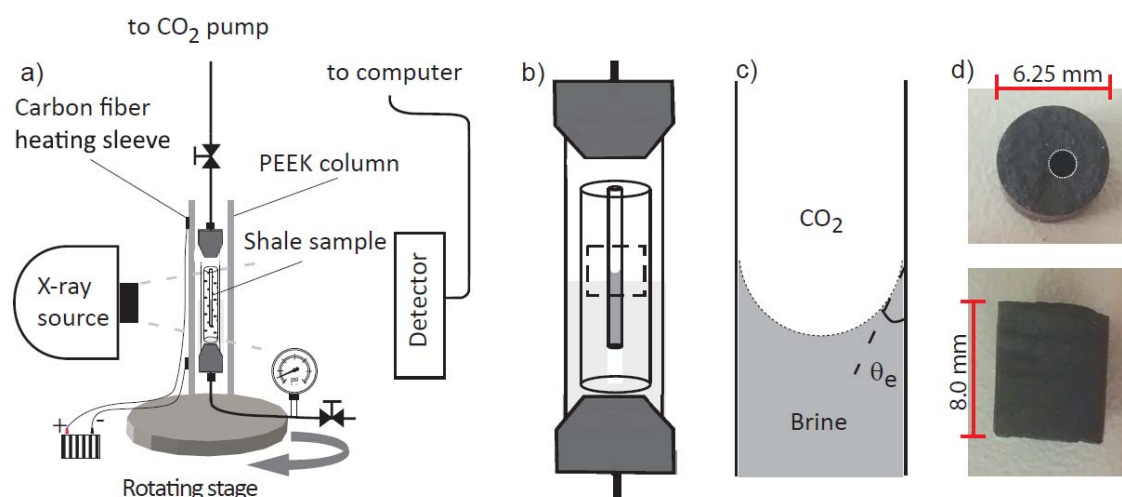
Figure 2.2: Experimental setup for X-ray computer tomography scanning of contact angle (modified from Tenney et al., 2017) (a,b) and example of sample core with capillary outlined by white dashed circle (c,d).

The samples were cleaned with a simple rinse of DI water. Unlike studies on representative minerals, we are investigating the bulk wettability of all the minerals and organic matter in this reservoir rock. Harsh cleansing agents could alter the surface chemistry of the organic materials. The Barnett Shale has been exposed to reservoir conditions and fluids on a geologic timescale. Thus, some inherent "contamination" is expected.

Once the shale sample preparation was completed, a 5 M NaBr brine was injected at ambient temperature and pressure using a syringe from the bottom of the capillary and stopped before reaching the top. Next, the brine-filled sample was placed into a poly-ether-ether-ketone (PEEK) pressure cell. The sample was then pressurized to 13.79 MPa with CO_2 (99.99% CO_2, AirGas Instrument Grade) using a supercritical fluid pump (SFT-10, Supercritical Fluid Technologies) and either left at room temperature (approximately 20° C) or heated to 40° or 60° C. A carbon fiber heating sleeve, pervious to X-rays and calibrated to the appropriate temperature, was used to heat the sample. Once heated and under pressure the brine and CO_2 were allowed to equilibrate for at least one hour while in contact with the shale sample. After imaging the samples at 13.79 MPa the pressure was released in increments of 1.72 MPa and the interface was reimaged. The technique is fully outlined in Chaudhary et al. [2015] and shown in Figure 2.2.

2.3.3 Image Acquisition and Processing

Digital radiographs were acquired on an X-ray microtomograph (Nikon X-TEK XT H 225). Each scan had an approximate resolution of 6 μm, with no filters used, a 1 frame per second exposure, energy current and power settings of approximately 57 kilovolts, 6.2 microamperes, and 10.9 watts. The average of two, 1-minute exposures, was used to correct for background noise.

Processing of the images was conducted using an algorithm developed in Matlab. First, a search window composed of the left and right wall and an upper and lower boundary are entered by the user. The algorithm then scans each pixel column of the image for the greatest average change in CT number across two 30-pixel vertical ranges stacked upon each other. By using a large search window, the approximate location of the interface can

18

be found despite the noise produced by the heterogeneity of the sample. Next two 5-pixel search windows were used to refine the interface detection. Finally, to limit the effect of noise that is located directly on the interface, a third 5-pixel window search is conducted where the curvature of the interface is enforced. Once the interface has been properly detected a circle is fit to these points using a least squares approach. Next, a tangent line to the circle is calculated at the point of intersection with the left wall and the angle between the tangent line and the left wall is found. In this approach, which is illustrated in Figure 2.3, the subjectivity of contact angle determination was reduced as much as possible. Precision of this method varies based on the image quality and mineral heterogeneity near the interface (which causes blotches in the CT image). The accuracy of this technique is similar to measurements in capillary tubes. Based on experience with interfaces of different degrees of sharpness we speculate that the precision is about ±5˚. An example of a synthetic capillary image with a contact angle of 13° was used to demonstrate the effect of noise on the interface detection (Figure 2.3). A raw example of the interface imaged at 13.79 MPa and 20° C from Tarrant#3-A at a depth of 1,880 meters is shown in Figure 2.4.
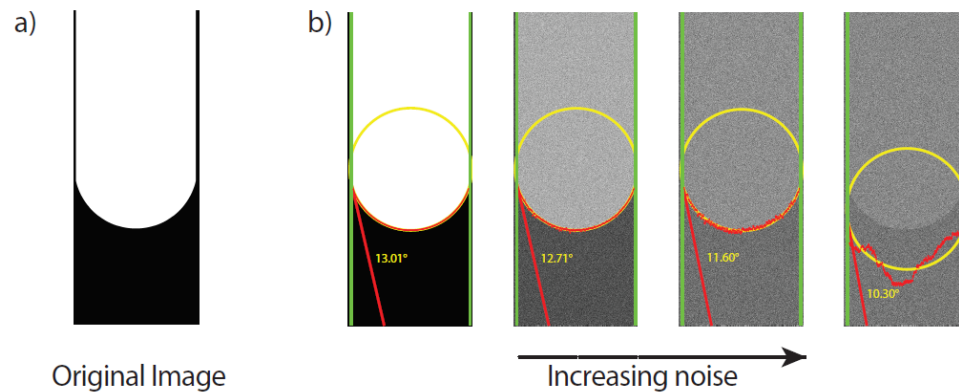
Figure 2.3: Accuracy of the interface detection with noise. (a) Synthetic capillary image with a 13° contact angle. (b) Interface and contact angle detection with increasing noise.
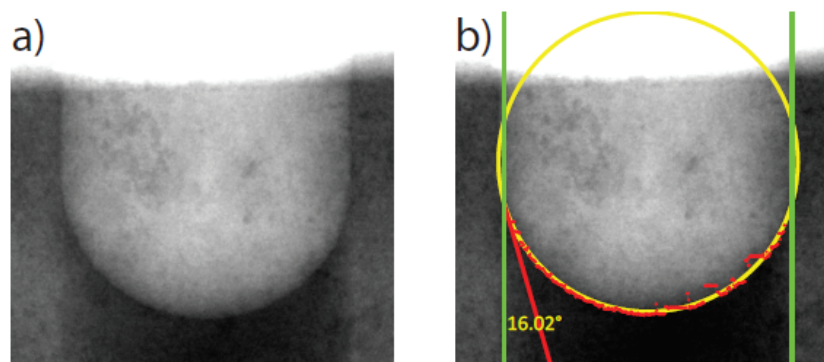
Figure 2.4: Illustration of raw and processed X-ray image: (a) raw image and (b) post processed image for interface detection and contact angle calculation. The green lines denote the shale surface picked, the red dots denote the fluid-fluid interface pixels detected, and the yellow circle denotes the circle fitted to the fluid-fluid interface. The resulting contact angle is shown in yellow.

2.3 RESULTS

All experimental results showed strong water-wet contact angles with the contact angle ranging from 6.8° to 29.4° (Figure 2.5 and Table 2.2). While there is no clear relationship between contact angle and vitrinite reflectance (Figure 2.5a), it is possible that samples with lower thermal maturities and higher thermal maturities are most water-wet; samples with intermediate thermal maturities are least water-wet. Samples from Young, W.C. #2 and Sims, T.P. #2 with vitrinite reflectance values 1.23 and 1.60 respectively showed the highest contact angle (Table 2.2). Lee, S #C-5-1 and Blakely #1, with vitrinite reflectance values of 0.58 and 2.16, respectively, showed the lowest contact angles. No discernible relationship between contact angle and TOC concentration was found (Figure 2.5b). The lowest average contact angle measured was in Blakely #1 ($\Theta = 10.3°$) with a TOC of 4.1%, while the highest average contact angle was in Young #2 ($\Theta = 17.5°$) with a TOC of 4.5% (Table 2.2).

20
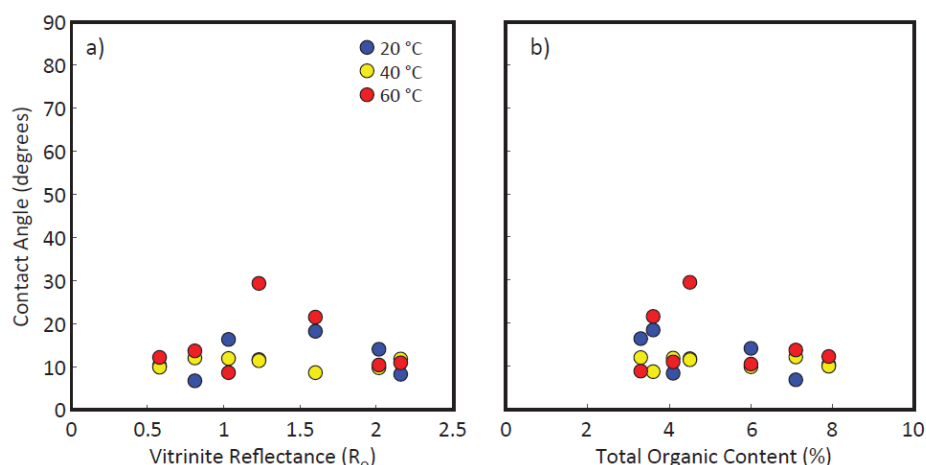
Figure 2.5: Contact angles of all Barnett Shale samples analyzed. (a) shows the contact angles versus vitrinite reflectance and (b) shows results of the same samples but plotted versus total organic carbon (mass%). The different colors correspond to different measurement temperatures.

Well	Depth (meters)	R_o (mass %)	TOC (mass %)	Contact Angle (°)		
				60° C	40° C	20° C
Sims, T.P. #2	2359.8	2.02	6	10.4	9.8	15.1
Sims, T.P. #2	2326.8	1.6	3.6	21.5	8.6	18.3
Young, W.C. #2	2108.6	1.23	4.5	29.4	11.4	11.7
Tarrant #3-A	1878.8	0.81	7.1	13.7	12.0	6.8
Tarrant #3-A	1880.0	1.03	3.3	8.7	11.0	16.3
Lee,S. #C-5-1	381.0	0.58	7.9	12.2	11.2	10.3
Blakely #1	2201.6	2.16	4.1	10.9	11.8	8.3

Table 2.2: Contact angle (Θ) measurement results for each sample amd different temperatures. Pressure is 13.79 MPa (2,000 psi). Temperatures are noted in the column label. R_o is vitrinite reflectance and TOC is short for total organic carbon. The well locations are shown in Figure 2.1.

Decreasing the pressure from 13.79 MPa had little effect on the contact angle (Figure 2.6; Table 2.3). Some researchers have noted an increase in contact angle with pressure; however, we did not see clear evidence of this phenomenon in our results. Four

out of seven samples displayed the highest contact angle at the highest measurement temperature of 60 °C. Increasing contact angle with temperature has been previously noted [Saraji et al., 2013; Sarmadivaleh et al., 2015].
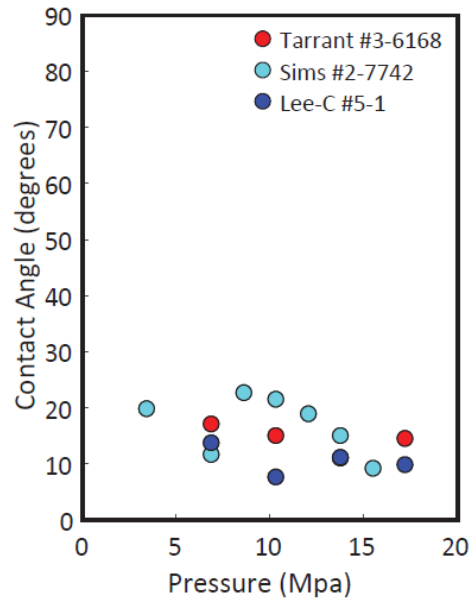
Figure 2.6: Contact angles measured during sequential depressurization of the pressure cell. The colors correspond to sample name and well location.

Sample	Pressure (MPa)	Contact Angle (°)
	3.4	19.9
	6.9	11.7
Sims #2	8.6	22.7
7742	10.3	21.5
20° C	12.1	18.9
	13.8	15.1
	15.5	9.3
Tarrant #3	6.9	17.2
6168	10.3	15.1
40° C	13.8	11.0
	17.2	14.5
	6.9	13.8
Lee-C #5-1	10.3	7.7
40° C	13.8	11.2
	17.2	10.0

Table 2.3: Results of contact angle (Θ) measurements during depressurization experiments.

Initially, our experiments were conducted with a brine similar to the Mt. Simon Formation's brine, a target for CO_2 sequestration in Decatur, Illinois, USA. However, we discovered that the contrast of the brine was not strong enough for the accurate detection of the interface with our algorithm. Instead a bromide-type brine was used to enhance the X-ray contrast between the brine and the shale. The 5 M NaBr concentration was selected to approximately match the ionic strength of the Mt. Simon brine. At a resolution of 6 μm, each 1.5 mm capillary was roughly 250 pixels in diameter. However, due to noise near the edges the best fit was accomplished by beginning the interface detection 10 pixels (60 μm) away from the left and right wall.

The supercritical point for CO_2 exists at 31.1° C and 7.39 MPa. No appreciable difference was noticed above and below the critical temperature or pressure. However, as CO_2 turned from liquid to gas during the depressurization experiments bubbles were formed within the brine which influenced the interface. While this measurement technique was developed for high pressure and temperature wetting experiments it could be used to measure low pressure CO_2 wetting, but this should be accomplished through a series of pressure increases to avoid CO_2 bubbles forming in the brine.

2.4 DISCUSSION

2.4.1 Effect of organic matter on shale wettability

Total organic concentrations within the range of an organic shale appear to have little to no effect on $scCO_2$ bulk wettability of Barnett Shale samples. Even though organic matter may become more oil-wet as it matures [Hu et al., 2016], organic shales are likely to remain water-wet with respect to CO_2. We hypothesize that this is due to the relatively low overall concentration of organic matter in organic shales. Even at 7.9% organic matter by weight, a relatively high concentration for shale, the wetting behavior of the shale is still controlled by the remaining mineral assembly. Assuming the organic matter and remaining mineral assembly have densities of 1.3 g/cc and 2.65 g/cc, respectively, the organic matter will account for 14.9% of the volume of the sample leaving the remaining 85.1% of the minerals to control the wetting behavior. However, it is important to remain cautious when applying these results to other organic shales. As the distribution of organic material in shale will vary from one shale to another it is important that further studies on organic shales are conducted.

24

The strongly water-wet nature of the Barnett Shale with respect to scCO$_2$ is an important finding for the prospects of geologic CO$_2$ sequestration. Using an average contact angle of $\Theta = 12.78°$ we can estimate the capillary entry pressure using the Young-Laplace equation (Eq. 2.1) and calculate the height of a CO$_2$ column (Eq. 2.3) which can be stored beneath an organic caprock like the Barnett. Assuming a median nanopore diameter for the Barnett of 100 nm [Loucks et al., 2009], an interfacial tension of 25.5 mN/M, the threshold pressure of this organic shale is about 1 MPa. Given a density difference of 300 Kg/m3 between brine and scCO$_2$, this translates to a scCO$_2$ column height of 338 m (Figure 2.7b).
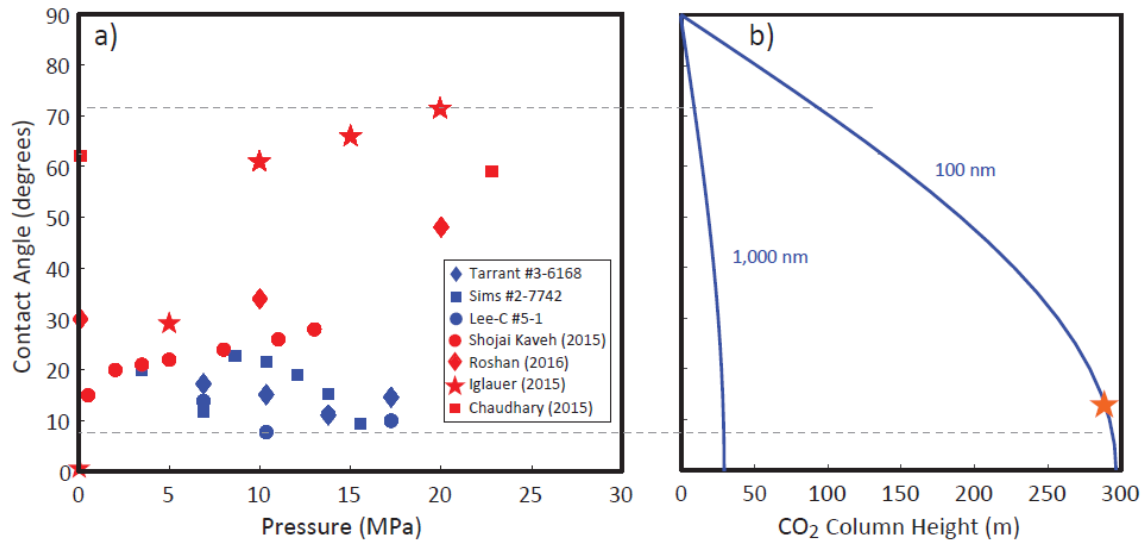
Figure 2.7: Contact angles of various shales taken from the literature (a) and the corresponding height of a continuous plume of CO$_2$ that can be held beneath a typical shale by capillary forces, idealized by a characteristic effective pore size, calculated as a function of contact angle (b). The orange star in (b) denotes the average of the measurements of Barnett Shale samples in this study. The dashed gray line denotes the full range as reported from literature.

2.4.2 Contact angle as a function of pressure

Our experiments did not show an increase in contact angle with pressure like some others have reported [Broseta et al., 2012; Chiquet et al., 2007; Iglauer et al., 2014, 2015a; Jung and Wan, 2012; Saraji et al., 2013]. According to Young's Law the contact angle between two fluids and a solid is a balance of the interfacial tensions between each fluid and solid pair. While the interfacial tension of CO_2 and brine decreases with pressure [Bachu and Bennion, 2009], which would cause the contact angle to decrease with pressure, however, this effect can be overridden by an increase in the interfacial tension between CO_2 and the solid minerals which is heavily dependent on the density [Al-Yeseri et al., 2016]. This density effect becomes muted at reservoir pressures as the density of CO_2 becomes less sensitive to pressure, which could explain the lack of an obvious trend in our data. Furthermore, our experiments were conducted while depressurizing the column, but other researchers typically measure with a "fresh batch" or by incrementally increasing the pressure. While this should have no effect on the interfacial tensions the possibility for hysteresis effects cannot be ruled out. Currently, our experimental setup does not allow for injecting brine under pressure.

2.4.3 Comparison with the capillary rise method

Initially we found our current results surprising given our previous measurements on a different organic shale [Chaudhary et al., 2015]. In an effort to explain the difference we conducted our experiments in the same manner as previously. That is, the synthetic capillary drilled in the sample was extended all the way through the sample. The sample was then placed into a PEEK column with brine at the bottom and the brine was allowed to rise due to capillary forces. This technique is equivalent to the capillary rise method

only visualized with a CT scanner. Conducting our experiments in this manner, we found

significantly higher contact angles (Figure 2.8).
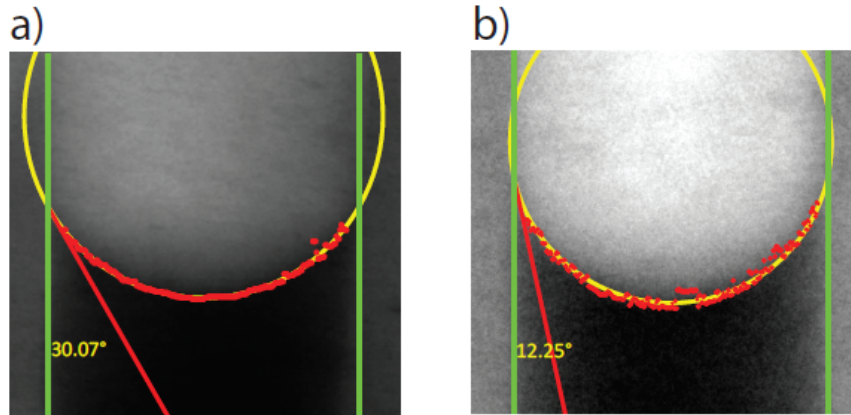
Figure 2.8: Comparison of processed X-ray images for a capillary drilled completely
through the sample (a) and a capillary that is partially drilled (b). In (a) the
brine is allowed to rise through the capillary while in (b) the brine is placed
within the partially drilled sample with a needle. Both experiments were
conducted at a pressure of 13.79 MPa (2000 psi) on the Lee, S. #C-5-1
sample. The green lines denote the shale surface picked, the red dots denote
the fluid-fluid interface pixels picked, and the yellow circle denotes the
circle fitted to the fluid-fluid interface. The resulting contact angle is shown
in yellow.

We hypothesize that by allowing brine to rise through the capillary, instead of being

placed in the capillary with a needle, we are preferentially measuring the most CO_2-wet

(although still slightly water-wet, in this case) area of the sample. The capillary forces

pulling the water up reach their minimum at this location and the movement of brine stops.

The organic matter within the Barnett is tied to organic rich laminations that extend

horizontally along bedding planes [Loucks et al., 2009]. This "mineralogical pinning" may

be the result of the laminated structure of our samples. We believe conducting experiments

in this manner is instructive because it illustrates the effect of mineralogical heterogeneity

on the wetting properties of the sample. It is unlikely, however, that these slightly water-

27

wet to mixed-wet areas will be continuous throughout a shale sample. Therefore, we expect areas of the sample that are strongly water-wet to be the dominant wetting characteristic of these samples and to be the main control on the potential flow of CO_2 through caprocks with similar mineralogy to the Barnett Shale.

2.4.4 Shale heterogeneity and organic matter distribution

We interpret our results as representative of the bulk wettability of the Barnett Shale. Our capillary method and the more common sessile drop method expose the CO_2 and brine to the entire mineralogy of the shale at the location of the interface. The contact angle formed is likely best described by the Cassie model [Cassie and Baxter, 1944] where the apparent contact angle, Θ_a, is proportional to the solid contact area, such that:

$$\cos(\theta_a) = f_1 \cos(\theta_{1,Y}) + f_2 \cos(\theta_{2,Y}) \hspace{2cm} (2.4)$$

where $\Theta_{1,Y}$ and $\Theta_{2,Y}$ are Young's contact angle on surface 1 and 2 and f_1 and f_2 are the ratio of liquid-solid contact area for each surface.

Shale porosity exists at the macro, micro, and nanoscale [Gerke et al., 2015]; however, only the mineralogy along the interconnected pore space is of importance for fluid flow. For some shales, like the Barnett, the pores are primarily located in the organic matter and for others the majority are within minerals [Loucks et al., 2009; Sondergeld et al., 2010]. Pores are often clustered together in groups of similar pore types with the smallest pores typically found in organic material [Akbarabadi and Piri, 2013; Milliken et al., 2013]. Pore interconnectedness does not extend throughout a sample or does so but only at the nanometer scale [Curtis et al., 2011; Gerke et al., 2015; Grathoff et al., 2016;

Hu et al., 2014]. This means that while isolated organic matter filled pores are likely CO_2-wet, they are not continuous, except perhaps at the nanoscale, and cannot feasibly transmit CO_2 across a shale caprock. The presence of cracks and fractures at the macroscale have the potential to be continuous but due to the patchy nature of the organic matter they are likely to remain water wet. This argument is consistent with the imbibition results of Akbarabadi and Piri [2013], where the larger inter-particle pores remain water wet despite the presence of smaller oil-wet organic matter pores. The predominant pore type within the Barnett shale are nanoscale intraparticle pores within the organic matter [Loucks et al., 2009]. These particles can have up to 20.2% intraparticle porosity with pores ranging from 5 to 750 nm with a median nanpore size of 100nm [Loucks et al., 2009] and the pore volumes may increase with increasing maturity [Sariento et al., 2014]. The organic matter is primarily located along horizontal laminations and is not continuous in the vertical direction [Loucks et al., 2009].Imbibition studies are perhaps the best way to analyze the wettability of the pore network, however they are difficult to perform at reservoir conditions with CO_2. Lan et al. [2015] conducted oil imbibition tests on the Motney and Horn River shales and found that even though both appeared oil wet during a droplet test, only the Motney shale imbibed more oil than water. They hypothesize that this is due to migrated liquid oil that substantially filled the pore network before physicochemical changes led to the precipitation of aggregate asphaltene which was followed by thermal cracking into bitumen lined pores. This suggests that understanding the depositional history and the source of organic materials plays an important role in the wetting of the pore network. The heterogeneity of shale means that despite the results of this work, and the few others that have studied CO_2 wetting on shales, there is still a need for more experiments, particularly on the mineralogical controls of wetting on different shales at various length scales.

2.5 CONCLUSIONS

This study shows that a range of TOC concentrations (3.27% to 7.88%) and thermal maturities (0.58 – 2.07 % Ro) have little effect on the wettability of an $scCO_2$ /brine/organic Barnett Shale system. We measured contact angles ranging from 6.8° to 29.4° at 20, 40, and 60° C and pressures ranging from 3.45 – 15.51 MPa and found little variation in the measured contact angle. Even at TOC concentrations as high as 7.9%, the wetting behavior of the remaining mineral assembly prevails in determining the macroscopic contact angle. When brine is allowed to rise through a capillary it displays a contact angle approximately 18° higher than when placed inside with a needle. This may demonstrate the influence of mineralogical heterogeneity on the wetting of the rock sample. Based on a compilation of all results we conclude that strong water-wet pores will retain buoyant CO_2 by capillary forces. The individual samples studied here show that organic shales, such us the Barnett Shale with patchy and laminated distribution of CO_2-wet organic material, have the potential to be suitable caprocks for CO_2 storage despite their mixed-wet nature. Other organic shales with higher TOC or a different distribution of organic matter deserve further characterization to determine sealing efficiency.

2.6 ACKNOWLEDGEMENTS

Chapter 3: Textural and Compositional Controls on Mudrock Breakthrough Pressure and Permeability

3.1 ABSTRACT

Breakthrough pressure and permeability control the structural sealing capacity of mudrocks at potential CO_2 sequestration sites and of hydrocarbon reservoirs. Breakthrough pressure studies on a variety of caprocks and similar geologic materials show a wide array of results due to the natural heterogeneity of mudrocks and the effects of variability in grain size distribution, fine sediment fraction, and mineral composition. Resedimentation techniques have been widely applied to the study of mudrock permeability but little work focused on breakthrough pressure. Here we perform a parametric study on breakthrough pressure and permeability in resedimented mudrocks using samples composed of ternary mixtures of kaolinite, quartz, and lime. We show that lime is effective in cementing resedimented samples, producing mechanically competent mudrocks and allowing for robust mercury injection capillary porosimetry. We observed that breakthrough pressure increases and permeability decreases with fine-grained void ratio, rather than bulk void ratio, according to power-law relationships. The fine-grained void ratio is defined as the ratio of the volume of voids to volume of fine grains where the size of the fine grains is controlled by the structure of the coarse-grained percolating network. These relationships can be used to estimate the sealing capacity of shaly sandstones and sandy mudrocks and highlight the variability of transport properties in coarse-fine sediment mixtures.

3.2 INTRODUCTION

The effort to mitigate climate change due to greenhouse gas emissions has been considered as the Apollo program of our time (King et al., 2015). One promising strategy is the permanent sequestration of anthropogenic carbon dioxide (CO_2) in deep saline reservoirs (Benson and Surles, 2006; Benson and Cook, 2005). Target reservoirs are often composed of massive sandstone formations (reservoirs) capped by low permeability shales (caprocks) (*Downey*, 1984; *Espinoza and Santamarina*, 2017) under which the CO_2 collects and remains trapped. Caprock integrity is also important when evaluating hydrocarbon reserves. If the reservoir pressure exceeds the sealing capacity of the caprock then, over geologic timescales, the reservoir will be depleted until the pressures are equilibrated with the capillary forces. Thus, the successful evaluation of hydrocarbon reservoirs and the security of CO_2 sequestration in deep geologic formations as a climate change mitigation strategy hinges on how well the caprocks function as seals.

The sealing capacity of a caprock directly depends on two related factors: how much pressure is needed for a nonwetting fluid (e.g., CO_2, oil, or gas) to break through the barrier and how much pressure builds up under the caprock. The pressure difference experienced at the caprock interface by a continuous buoyant nonwetting plume with height *h* is:

$$\Delta P = (\rho_b - \rho_g)gh \qquad (3.1)$$

where ρ_b is the brine mass density, ρ_g is the nonwetting phase mass density, and g is the gravitational acceleration, and *h* is the height or thickness of the nonwetting plume, usually referred to as the CO_2/oil/gas column (*Peters*, 2012; *Schowalter*, 1979). The breakthrough pressure (P_c*), or displacement pressure, of a given porous medium can be theoretically calculated using the Young-Laplace equation (*Laplace et al.*, 1829; *Young*, 1805):

$$P_c^* = \frac{2\sigma \cos(\theta)}{r_c^*} \tag{3.2}$$

where θ is the contact angle of formation brine in the presence of the nonwetting fluid, σ is the interfacial tension between the brine and the nonwetting fluid and r_c^*, the critical pore radius, is the minimum pore radius along an interconnected and continuous path of pores across the porous medium at breakthrough.

Mercury intrusion capillary porosimetry is widely used in the oil industry to investigate entry pressure, breakthrough pressure, and estimate the permeability of porous media. This method utilizes the Laplace equation and an understanding of the contact angle of mercury to develop a pore throat distribution. Once this pore throat distribution is known, an assumed contact angle can be used to estimate the entry pressure and breakthrough pressure of any fluid. This technique is easy to run and readily reproduce making it ideal for conducting a large number of breakthrough pressure experiments. The disadvantages of this technique are due to the uncertainties in contact angle and the possibility for shrinking of clays during the drying processes. For these reasons, the best way to establish definitive breakthrough pressures of CO_2 in a particularly shale is through CO_2 breakthrough pressure experiments. In this paper, we present our results in terms of CO_2, however our goal is to understand the fundamental controls on breakthrough pressure of all fluids and not the absolute value of any one particular sample.

CO_2 breakthrough pressure measurements on a variety of natural formations range from approximately 0.1 MPa to 5 MPa (*Harrington et al.*, 2009; *Hildenbrand et al.*, 2002; *Hildenbrand et al.*, 2004; *Wollenweber et al.*, 2010). Evaporites exhibit some of the highest breakthrough pressures with values as great as 21 MPa for CO_2 (*Li et al.*, 2005). CO_2 breakthrough pressure experiments on resedimented samples, have shown that r_c^* (Eq. 3.2) is generally larger than the mean pore throat radius in homogeneous porous media (*Espinoza and Santamarina*, 2010). A summary of recent breakthrough pressure

experiments highlights the role of particle size distribution and specific surface on P_c^* (*Espinoza and Santamarina*, 2017; *Makhnenko et al.*, 2017).

Breakthrough pressure plays an important role in the Sleipner CO_2 sequestration project in the North Sea, for example, where nearly a million tons of CO_2 have been injected each year since 1996 (*Arts et al.*, 2004; *Chadwick et al.*, 2010). Monitoring of the CO_2 plume with 4D seismic surveys reveal that the plume has ascended rapidly through eight thin shaly barriers at unexpectedly low breakthrough pressures before being trapped beneath a large competent caprock (Cavanagh and Haszeldine, 2014). This unexpected plume behavior suggests that some properties of the CO_2 plume barriers have not been accurately characterized. The causes for such phenomenon partly originate on the spatial variability and heterogeneous nature of mudrocks. Mudrocks are usually recognized by its amount of clay minerals in the rock matrix. Typically well logging measurements, such as gamma ray emission and spontaneous potential, measure bulk volume fractions of clay content in shaly sediments, but cannot tell the location of clays within the rock matrix and their effect on transport properties (*Peters*, 2012). Hence, it is not straightforward to assess the sealing capacity of shaly sandstones or sandy shales from gamma ray or spontaneous potential only. The study of synthetic resedimented mudrock samples helps understand better these sediment mixtures.

Resedimentation is the process by which slurries are incrementally compressed to high effective stress under oedometric conditions (one-dimensional strain) to mimic the sedimentation process *Germaine and Germaine,* 2009). The process can be used to create synthetic mudrocks with prescribed mineralogy, grain size, and a target porosity or effective stress. The creation of resedimented mudrocks allows for the systematic study of a single factor such as the mineral composition, grain size, or effective stress, thus reducing the variability produced by the study of natural materials (*Schneider et al.*, 2011).

Resedimentation experiments have been used to explore permeability, porosity and compressibility as a function of mineralogical composition, however, generally employing a narrow grain size distribution and/or low effective stress as required for studying deep mudrocks (*Bandini and Sathiskumar*, 2009; *Dewhurst et al.*, 1999; *Dewhurst et al.*, 1998; *Espinoza and Santamarina*, 2017; *Mondol et al.*, 2008; *Mondol et al.*, 2007; *Reece et al.*, 2013; *Schneider et al.*, 2011; *Shafiee*, 2008). For example, *Schneider et al.* (2011) used resedimentation techniques on a natural illitic mudrock that was mixed with silt-sized silica to create five different mixtures ranging in composition from 36% to 57% clay by weight. Each sample was consolidated to a maximum vertical effective stress of 2.4 MPa and vertical permeability was calculated assuming a constant strain-rate during consolidation increments. Scanning electron microscopy (SEM) analysis of these samples showed that the silt sized silica grains formed "silt bridges" which allowed for increased permeability with decreasing clay fraction. They proposed a dual porosity model where the clay and silt fractions have separate permeabilities which contribute to the overall effective permeability.

Espinoza and Santamarina (2017) used resedimentation experiments to explore breakthrough pressure in sediments with CO_2. The authors consolidated homogenous specimens of fine sand, calcium carbonate, kaolinite, and montmorillonite to a maximum effective stress of 3 MPa within a spring-loaded oedometer flow-through cell. They found that breakthrough pressure corresponded with pore throats larger than the mean for their specimens with breakthrough pressures ranging from 0.11 MPa in silt-sized calcium carbonate to a maximum of 3.0 MPa in pure montmorillonite clay. However, their work did not explore various sediment mixtures which is more representative of real mudrocks. *Makhnenko et al.* (2017) conducted CO_2 breakthrough pressure experiments on a

resedimented opalinus clay and found good agreement between resedimented and natural samples.

Our work presented here builds on that of *Espinoza and Santamarina* (2017) and *Schneider et al.* (2011), as well as other previous studies of resedimented mudrocks by exploring the effect of mixtures of quartz, kaolinite, and lime on the transport properties of mudrocks. These are representative of typical constituents of mudrocks – fine siliciclastic grains (represented by quartz), clay (kaolinite) and a carbonate cement (lime). By mixing three minerals into our slurries we produce samples with varied mineralogy, porosity, and pore structure. This helps achieve our goal of developing predictive relationships between mineral composition and grain texture with mudrock permeability and breakthrough pressure simultaneously. Here, for the first time, we analyze the breakthrough pressure of controlled sediment mixtures consolidated to high effective stresses. In addition, permeability from mercury injection capillary porosimetry and consolidation techniques are estimated for the same samples. We synthesize the results by regression and then compare them to previous work.

3.3 EXPERIMENTAL METHODS

3.3.1. Materials, Consolidation Technique and Permeability Estimation

Three types of sediments were used: fine grained quartz, hydrated lime, and kaolinite (Table 3.1). The quartz was supplied by Allied Compounds and passed a 200 mesh (74 μm). The hydrated lime was supplied by Aqua Phoenix Scientific with 94% passing a 325 mesh (44 μm) and 99% passing a 200 mesh. A hydrometer was used to measure the particle size distribution for each mineral component according to ASTM D7928 (Figure 3.1). A high powered commercial blender (Waring Model # 37BL19) was

used to mix the slurries with a 5 M ionic strength brine composed of sodium chloride, calcium chloride, magnesium chloride, potassium chloride, and potassium bromide. This brine approximately matches the brine in the Mount Simon formation, a potential target for CO_2 geologic storage (*Botto et al.*, 2017).

Sample ID	Mineral Fraction (% Volume)			Initial Porosity of Slurry (%)
	Quartz	Kaolinite	Lime	
1	100	0	0	43
2	75	25	0	51
3	75	0	25	60
4	60	20	20	60
5	50	50	0	49
6	50	0	50	61
7	40	40	20	61
8	40	20	40	61
9	25	60	15	60
10	25	0	75	66
11	20	80	0	65
12	20	60	20	65
13	20	40	40	65
14	20	20	60	65
15	0	100	0	63
16	0	80	20	69
17	0	70	30	67
18	0	40	60	68
19	0	20	80	70
20	0	0	100	70

Table 3.1: Mineralogical composition of slurries created for incremental consolidation
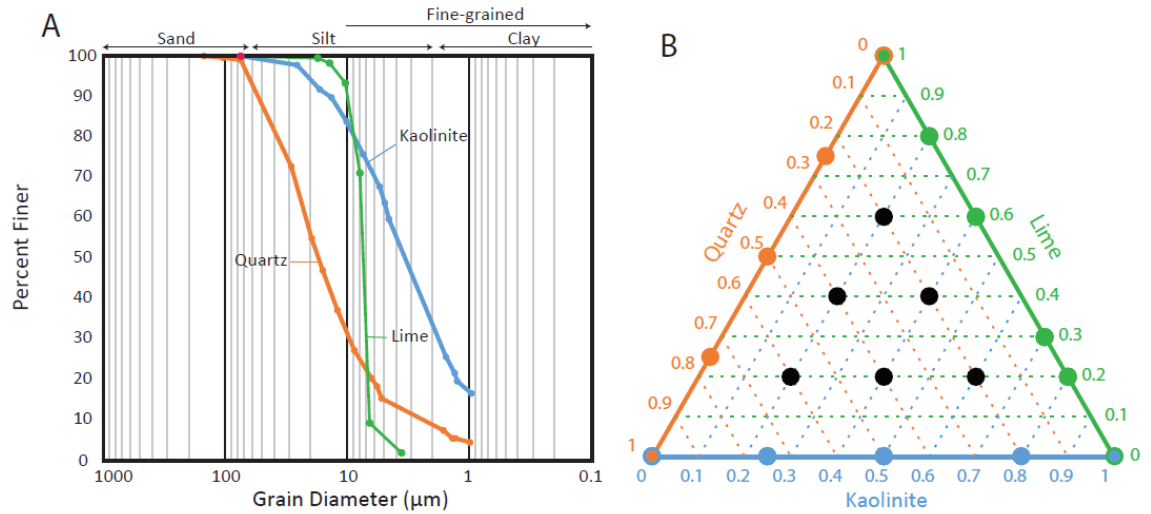
Figure 3.1: (A) Grain size distribution of mineral powders used to create resedimented mudrocks samples. (B) Ternary compositional diagram of all samples created and tested.

Next, the slurry was loaded into the oedometer consolidation device (1D strain deformation) for incremental stress loading (Figure 3.2). The small diameter of the consolidation device allows for high effective stresses to be achieved without the use of a large hydraulic press. In this case the application of 12 Kg of weight with the lever arm set to a 10:1 multiple results in 36 MPa of effective vertical stress. Sixteen stress increments were conducted beginning at 0.015 MPa and doubled until reaching 36 MPa for all samples. Displacement was monitored with a linear displacement transducer to ensure that primary consolidation (pore pressure dissipation) was complete before the next stress increment was begun. An example of the strain-time series signature is presented in Figure 3.3a. The log-time, outlined in detail in *Germaine and Germaine* (2009), was used to identify the end of primary consolidation (Figure 3.3b).
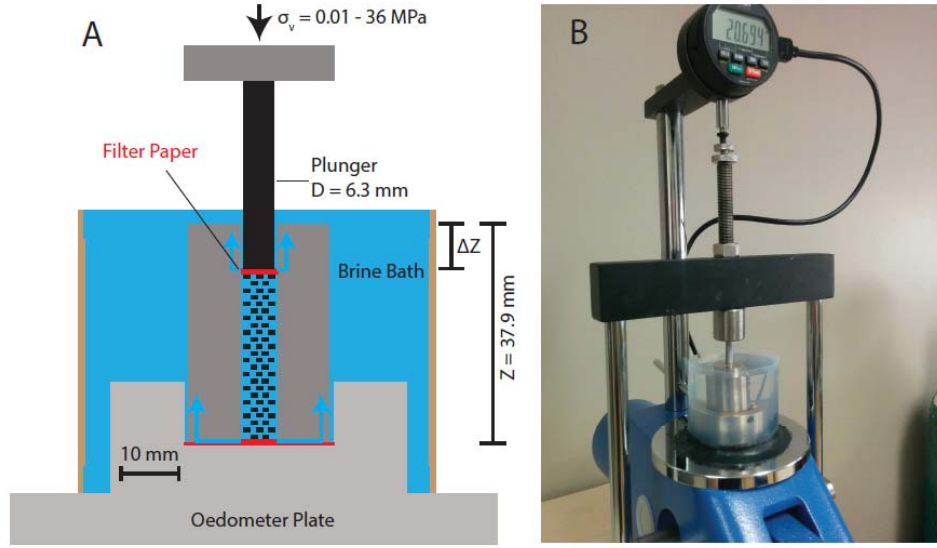
Figure 3.2: (A) Diagram of consolidation apparatus. The blue arrows indicate direction of pore water flow during consolidation. (B) Picture of the apparatus during consolidation and oedometer testing.
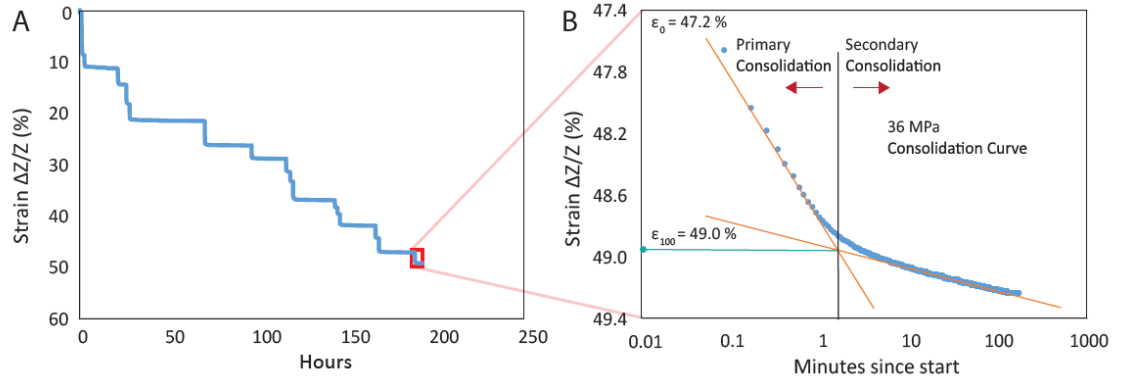
Figure 3.3: (A) Example of a consolidation curve. (B) Zoomed-in portion of incremental strain where $\varepsilon 0$ and $\varepsilon 100$ correspond to the strain at 0 and 100% primary consolidation.

3.3.2 Mercury Injection Capillary Porosimetry

Mercury injection capillary porosimetry (MICP) was conducted on each sample using a Micromeritics AutoPore IV 9500 device. Before MICP, each sample was oven

39

dried for 24 hours at 80° C. Pressure was incremented in 53 steps up to a maximum of 413.7 MPa (60,000 psi; Figure 3.4a). Pore size distributions were calculated using the Young-Laplace equation (Eq. 3.2), a contact angle for mercury of 130°, and an interfacial tension of 0.485 N/m. Permeability was estimated using the modified Purcell's model (*Purcell*, 1949) where the capillary tubes are exchanged for sheets (*Brown*, 2015) and with a lithology factor of 0.085, the minimum calculated by Purcell. The lithology factor represents the tortuosity of the tubes, or sheets, and is lowest in mudrocks. $P_c{}^*$ and $r_c{}^*$ were determined by fitting a curve to the cumulative intrusion data plotted against the logarithm of pressure. The point of greatest slope on this curve corresponds to $P_c{}^*$ and $r_c{}^*$ (*Katz and Thompson,* 1987) and is located at the local minimum of the second derivative of the curve (Figure 3.4b-c).
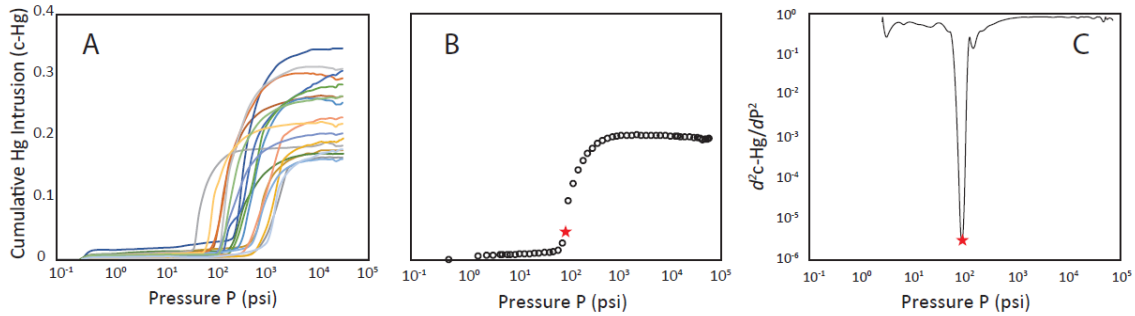
Figure 3.4: (A) All mercury intrusion experiments conducted in this study. (B) Typical example of an individual mercury intrusion curve with red star marking $P_c{}^*$ at the inflection point. (C) Second derivative of curve fitted to data in B in logspace. The red star marks the inflection point.

In our experiments entry pressure was selected as the first point which deviated from the initial straight line portion of the MICP curve. The pressures observed during MICP only apply to the liquid/vapor mercury system. Pressures were converted to brine/CO_2 capillary

pressures by scaling with the ratio of interfacial tensions and contact angles (*Schowalter*, 1979):

$$P^*_{c_{CO2}} = P^*_{c_{Hg}} \frac{\sigma_{b/CO2}\cos(\theta_{b/CO2})}{\sigma_{Hg}\cos(\theta_{Hg})} \tag{3.4}$$

where $\sigma_{b/CO2}$ and σ_{Hg} are the interfacial tensions between brine/CO_2 and liquid/vapor mercury, respectively, and $\theta_{b/CO2}$ and θ_{Hg} are the contact angles between brine/CO_2 and mercury. For this study we assumed that CO_2 is completely non wetting with respect to brine, ($\theta_{b/CO2}$ was assumed to be 0°). $\sigma_{b/CO2}$ is strongly dependent upon pressure and temperature. For these experiments we assumed a reservoir temperature of 60° C and 13.8 MPa (2,000 psi) which results in a $\sigma_{b/CO2}$ of approximately 0.030 N/m (*Bachu and Bennion*, 2009).

3.4 RESULTS

Table 3.2 and Figure 3.5 summarize the mineralogical compositions of the resedimented samples, the CO_2 entry pressure, breakthrough pressure, and permeability from MICP analysis. The edges of the ternary diagrams represent two-component mixing lines (e.g., the lower edge of the ternary triangle corresponds to mixtures moving from 100% quartz at the lower left to 100% kaolinite at the bottom right) and are displayed in Figure 3.5 (D-F).
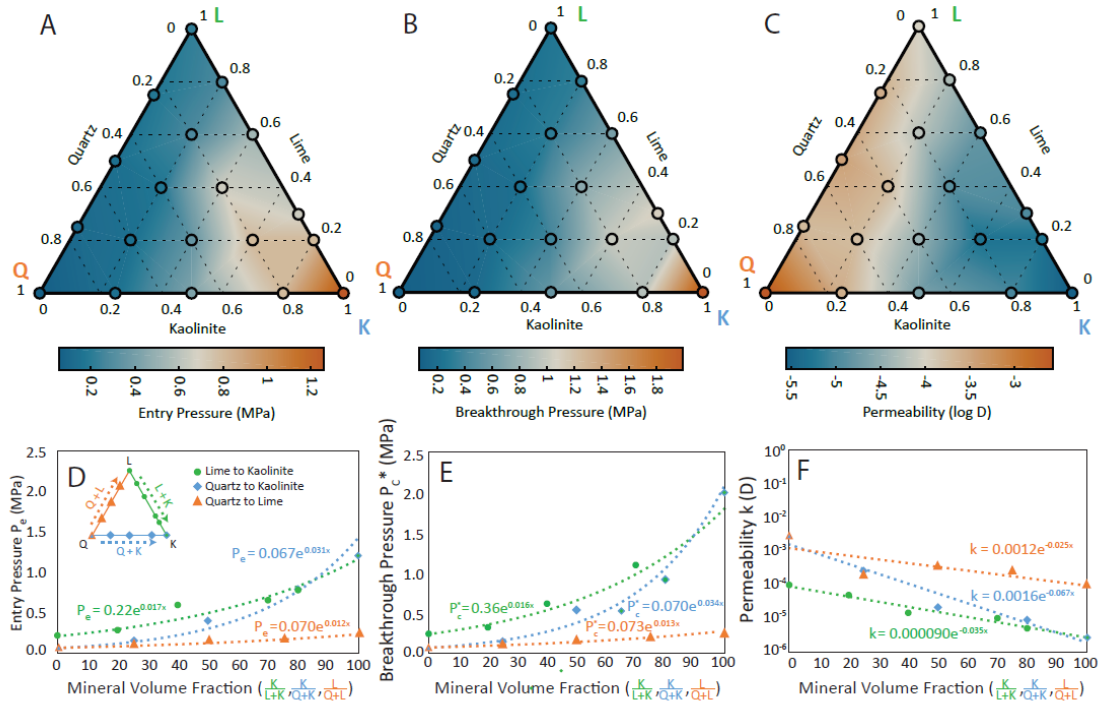
Figure 5. (A) CO$_2$ entry pressure , (B) CO$_2$ breakthrough pressure, (C) permeability for all the samples created and analyzed. The corresponding two-component samples are shown in (D)-(F) along with results of an exponential fit

Figure 3.5: (A) CO$_2$ entry pressure, (B) CO$_2$ breakthrough pressure, (C) permeability for all the samples created and analyzed. The corresponding two-component samples are shown in (D)-(F) along with results of an exponential fit.

Sample ID	Mineral Fraction (% Volume)			Porosity during MICP (%)	Entry Pressure of CO_2 (MPa)	Breakthrough Pressure of CO_2 (MPa)	Permeability (D)
	Quartz	Kaolinite	Lime				
1	100	0	0	31	0.06	0.06	2.7E-03
2	75	25	0	28	0.14	0.15	2.6E-04
3	75	0	25	34	0.11	0.11	1.9E-04
4	60	20	20	33	0.14	0.17	1.8E-04
5	50	50	0	24	0.42	0.54	2.1E-05
6	50	0	50	38	0.14	0.16	3.6E-04
7	40	40	20	33	0.34	0.38	3.6E-05
8	40	20	40	39	0.18	0.20	1.9E-04
9	25	60	15	31	0.34	0.41	5.1E-05
10	25	0	75	41	0.18	0.20	2.6E-04
11	20	80	0	26	0.79	0.92	9.1E-06
12	20	60	20	28	0.79	1.00	5.1E-06
13	20	40	40	33	0.65	0.71	1.3E-05
14	20	20	60	37	0.28	0.31	6.2E-05
15	0	100	0	22	1.26	1.99	2.8E-06
16	0	80	20	32	0.79	0.91	5.1E-06
17	0	70	30	27	0.66	1.10	1.0E-05
18	0	40	60	35	0.53	0.62	1.5E-05
19	0	20	80	40	0.28	0.32	4.9E-05
20	0	0	100	43	0.22	0.24	9.9E-05

Table 3.2. Mineralogical composition of the consolidated samples and the results of MICP interpretation. Converted from $\theta_{b/CO2}$ = 0°, σb/CO2 = 0.03 N/m, θ_{Hg} = 130°, σHg = 0.485 N/m (Eqt 3.4).

3.4.1 Entry Pressure

Entry pressure (P_e) is the pressure necessary to enter the largest pore throats accessible on the perimeter of the sample. Our results show a wide range of entry pressure from 0.06 MPa in the 100% quartz sample to 1.26 MPa in the 100% kaolinite sample (Figure 3.5A). These pressures correspond to the largest pore throat diameters in the samples which are 1.04 μm for pure quartz, 0.05 μm for pure kaolinite, and 0.28 μm for

pure lime. Entry pressure generally decreases with the addition of kaolinite and lime (Figure 3.5A). Two-component mixing experiments reveal exponential relationships between each mineral pair as a function of volume fraction (Figure 3.5D). Entry pressure increases most rapidly along the quartz-to-kaolinite mixing line while the quartz-to-lime relationship is nearly linear.

3.4.2 Breakthrough Pressure

The breakthrough pressure ranges from 0.06 MPa in the pure quartz sample to 2.0 MPa in the pure kaolinite sample (Figure 3.5B). This corresponds to a range of $r_c^* = 0.93$ µm to 0.03 µm. The three-component mixtures are most strongly controlled by the concentration of kaolinite and to a lesser degree the concentration of lime. In the two-component samples, the breakthrough pressure is exponentially related to increasing kaolinite or lime concentration with the greatest increase along the mixing line from 100% quartz to 100% kaolinite (blue dashed line in Figure 3.5E). The complex response of multi-component mixtures emphasizes the need to look beyond two-component mixtures when studying transport behavior in resedimented samples.

3.4.3 Permeability

Permeability ranges over three orders of magnitude from a high of 2.7 mD ($2.7{\times}10^{-15}$ m^2) in the 100% quartz sample to 2.8 µD ($2.8{\times}10^{-18}$ m^2) in the 100% kaolinite sample (Figure 3.5C). Permeability generally decreases as the volume fraction of lime and kaolinite increases. Lime mixtures are generally less permeable than quartz mixtures. Two-component mixing line results reveal an exponential relationship between the mineral pairs with the permeability decreasing the greatest along the quartz to kaolinite mixing line (Figure 3.5F). In three-component samples, there is no discernible correlation to any one

mineral concentration which highlights the need to explore other parameters, such as void ratio and clay fraction.

3.5 DISCUSSION

3.5.1 Suitability of Mercury Intrusion to Estimate Transport Properties on Uncemented and Fine-grained Sediments

Permeability and entry pressure of mudrocks can be difficult to estimate during MICP due to conformance and compressibility errors (*Comisky et al.*, 2011; *Peng et al.*, 2017). Conformance errors are due to surface vugs, large grains, and irregularities at the surface, and are limited when using whole, non-crushed, samples (*Peng et al.*, 2017). For the purposes of this study we assume conformance issues are negligible. During the early phase of MICP, compression errors occur when the voids not yet intruded by mercury begin to compress in response to the increased exterior capillary pressure. At high pressure compression errors occur due to compression of organic material and other low density materials (*Peng et al.*, 2017). Due to the lack of cementation, resedimented samples are likely to experience erroneous prediction of capillary entry due to compressibility errors. To prevent this artifact, we created calcite cementation through the use of hydrated lime during the consolidation process. However, our samples are still subject to some early compression, particularly in samples without lime. To correct for this artifact we assume all mercury intrusion prior to the selected entry pressure is due to compression and is subtracted from the cumulative intrusion curve.

Civil engineering applications often use hydrated lime to stabilize soils (*Sherwood*, 1993). Hydrated lime converts to water and calcium carbonate by absorbing CO_2 from air. Here, we use this process to create cemented sediments without the unnatural silicates found in concrete. Unlike resedimented samples without lime, our samples remain

45

competent even when saturated with water. This trait could prove useful for further flow and transport investigations as well as mechanical studies. After consolidation was complete, environmental scanning electron microscopy paired with energy dispersive X-ray spectroscopy (SEM-EDS) was used to examine the fabric of the rock (Figure 3.6).
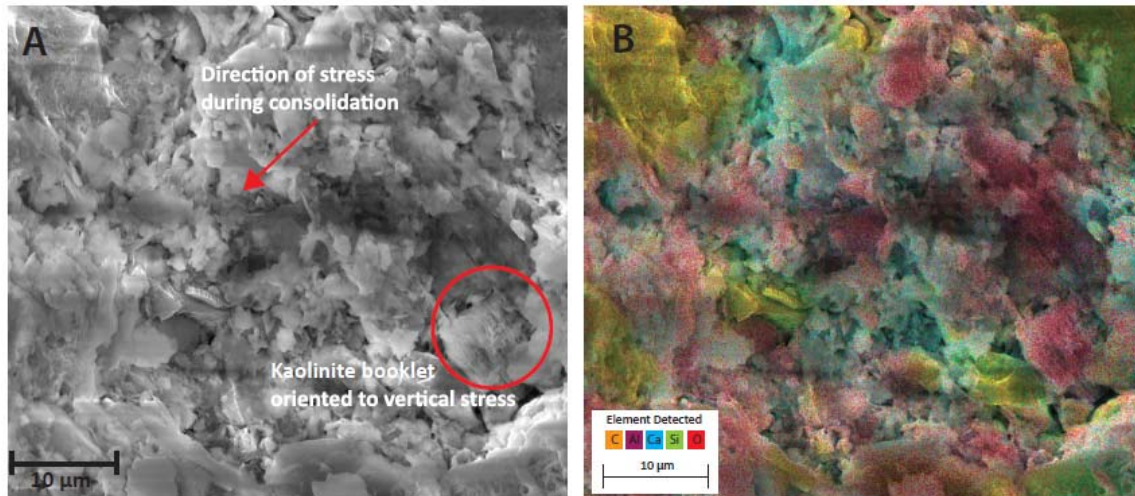
Figure 3.6. (A) Scanning electron microscope image of a resedimented sample and corresponding (B) energy dispersive x-ray spectroscopy result. The sample mineralogical composition is 25% quartz, 60% kaolinite, and 15% lime.

Spectroscopy revealed the alignment of clay platelets with the direction of vertical stress during consolidation in agreement with previous observations (*Adams et al.*, 2013; *Day-Stirrat et al.*, 2011; *Schneider et al.*, 2011). EDS imaging revealed carbon and calcium signatures present throughout the matrix which corresponds to the lime/calcite. The addition of lime helps strengthen the resedimented samples and decreases compression during the initial phase of MICP. A comparison of two high-clay content samples, one created with hydrated lime and one without, shows the difference between samples created with and without cementation (Figure 3.7).
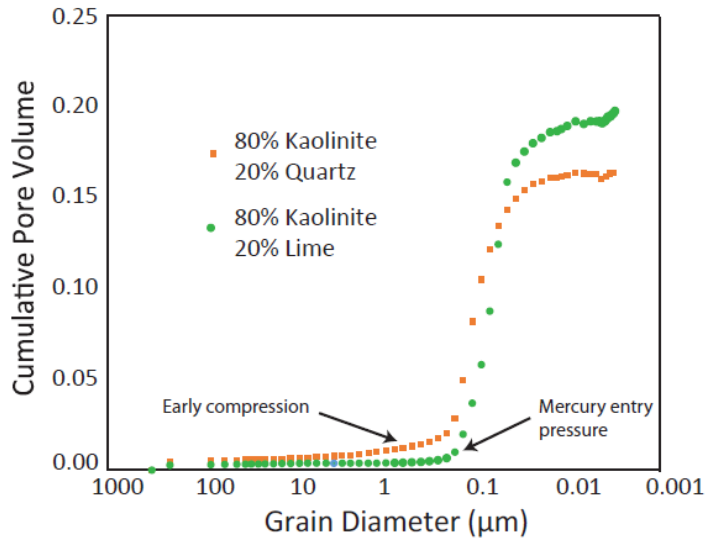
Figure 3.7: Comparison of cumulative intrusion curves for similar 80% kaolinite samples, but one mixed with quartz and the other mixed with lime. The sample with lime experiences significantly less compression before entry of mercury.

Another artifact introduced by MICP measurements is pore structure alteration induced by oven-drying. Capillary forces during drying can move fine grained sediments to grain contacts and pore throats and induce capillary-driven cracks (*Shin and Santamarina*, 2011). We limit this process through our use of kaolinite, a non swelling clay, however it cannot be discounted entirely. Despite some of the mentioned artifacts involved in MICP, these type of measurements are extremely useful to perform parametric studies with a large number of samples. Section 3.5.3 discusses a comparison of the results in transport properties derived from MICP with other methods.

3.5.2 Fine Grained Control on Transport Properties

The void ratio (*e*) quantifies the space available in a sediment for flow or compression and is proportional to porosity (e $= \frac{\varphi}{1-\varphi}$) (*Germaine and Germaine*, 2009).

The void ratio of a sample is defined as the volume of voids (V_v) divided by the total volume of solid grains (V_s). Here, we find it insightful to define a fine-grained void ratio (e_f, *Schneider et al.,* 2011)

$$e_f = \frac{V_v}{V_{sf}}$$ (3.5)

where V_{sf} is the volume of "fine grains". Similarly, a coarse-grained void ratio (e_c) can be defined as

$$e_c = \frac{V_v + V_f}{V_{sc}}$$ (3.6)

where V_{sc} is the volume of "coarse grains". The definition of e_c differs from the typical definition of void ratio because it includes the volume of voids and volume of fines in the numerator. This ratio represents how tightly packed the coarse grains are within the sample. A clean sandstone can have a porosity of approximately 33% which corresponds to $e_c = 0.5$; therefore, 0.5 should be considered the approximate lower bound for e_c and the point at which the entire skeleton is composed of coarse grains in contact with one another (Figure 3.8A). *Schneider et al.* (2011), show that in sediments with silt fractions of 43% and consolidated to 2.4 MPa the coarse grains disturb the alignment of fine-grains and contribute to permeability. *Jung et al.* (2012) propose that above a critical fines content permeability decreases to the permeability of fines. In our experiments no particular dependence on e_c is apparent, instead e_f appears to control the transport properties of our samples throughout the range tested. This is apparent in the breakthrough pressure bubble plot shown in Figure 3.8.
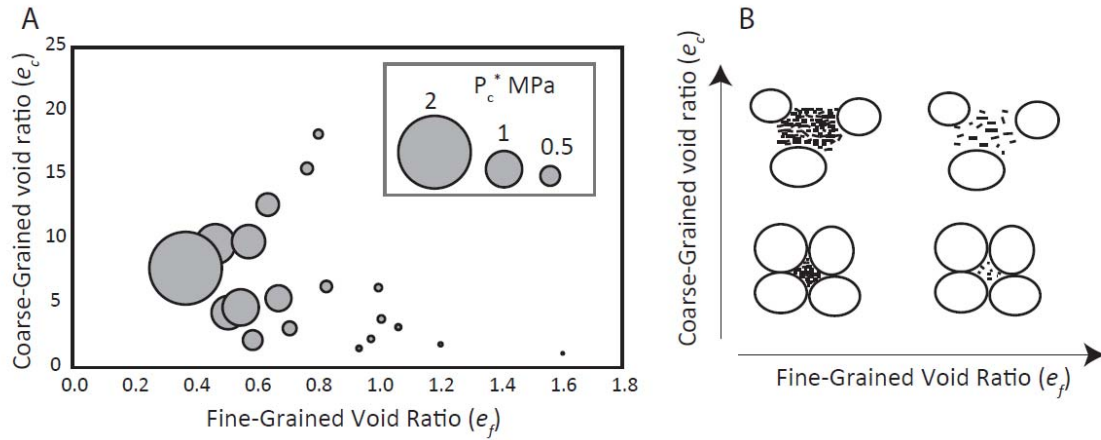
Figure 3.8: (A) Breakthrough pressure bubble plot. (B) Schematic of grain distribution at different fine-grained and coarse-grained void ratios.

The fine-grained void ratio defined above is similar to the void ratio of the clay fraction defined by *Schneider et al.* (2011); however, we do not define V_f as the volume of grains that are clay sized. In these experiments we find that V_f chosen as the volume of grains smaller than 10 µm yields a suitable power law relationship between P_c^* and e_f (Figure 3.9a). Figure 3.9b shows the results of an error analysis where the fine-grained void ratio was recalculated using different grain size diameter cutoffs and power law functions were fit to the corresponding P_c^* and e_f distributions. The best correlation (R^2 closest to 1) occurs at 10 µm.
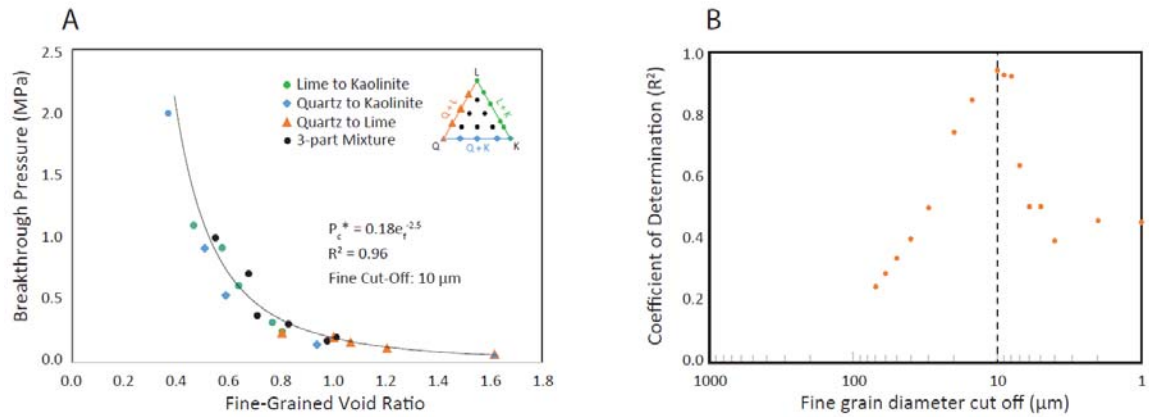
Figure 3.9: (A) Breakthrough pressure as a function of fine-grained void ratio. (B) Coefficient of determination (R^2) for power models (such as in A) depending on which fine-grained diameter cut off criterion is used.

We justify the use of 10 μm from a fundamental standpoint by observing that the breakthrough radius, or critical pore radius r_c*, of the pure quartz sample is 0.9 μm. Critical path analysis reveals that the transport properties of porous media are primarily controlled by pores which are have a radius equal or greater than r_c* (*Daigle*, 2016). In sandstones, the aspect ratio of pore throats to pore bodies ranges from 5:1 to 10:1 (*Hartmann and Beaumont*, 1999). This means that the percolating pore network of our pure sand sample is most strongly controlled by pore throats that are 1.8 μm in diameter and pore bodies that are approximately 9 to 18 μm (Figure 3.10).
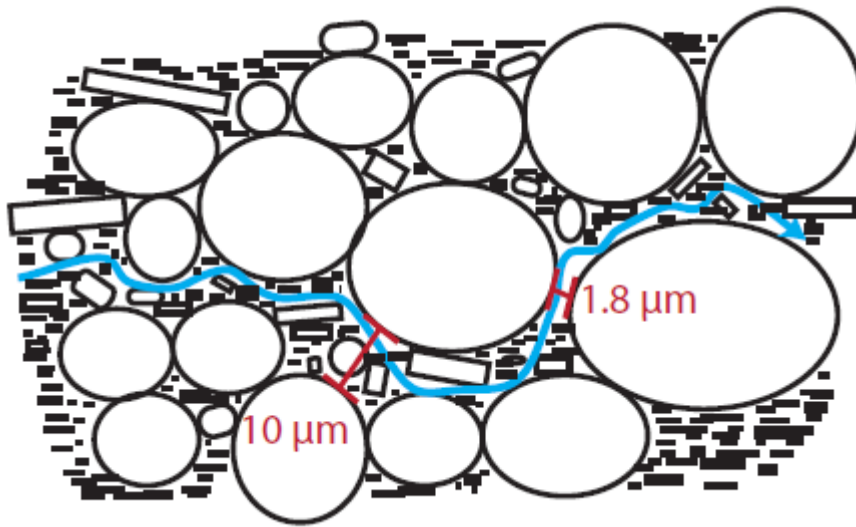
Figure 3.10: Schematic illustration of pore structure where an interconnected pathway of pore throats and bodies between coarse grains contains some fine grains.

In samples that are not pure sand we still expect a similar coarse grained pore network to form as the coarse grained void ratio approaches the lower limit. However, in these samples the network may be partially filled with grains < ~10 μm in diameter. We hypothesize that the grain diameters which are larger than the pore bodies of the percolating network do not have a significant influence on the advective transport properties of these samples. Therefore, the coarse grains within a mudstone determine the structure of the percolating network while the void ratio within the network controls the breakthrough pressure.

3.5.3 Comparison of MICP Transport Properties with Other Methods

Permeability: *Crawford et al.* (2008) consolidated mixtures of fine grained quartz and kaolinite to 50 MPa to evaluate the permeability of fault gouge. They measured permeability using water at high permeability and argon on the lower permeability samples.

51

Our mixtures from quartz to kaolinite are very similar to these samples and our permeability estimates using Purcell's theory agree very closely with their permeability measurements (Figure 3.11).
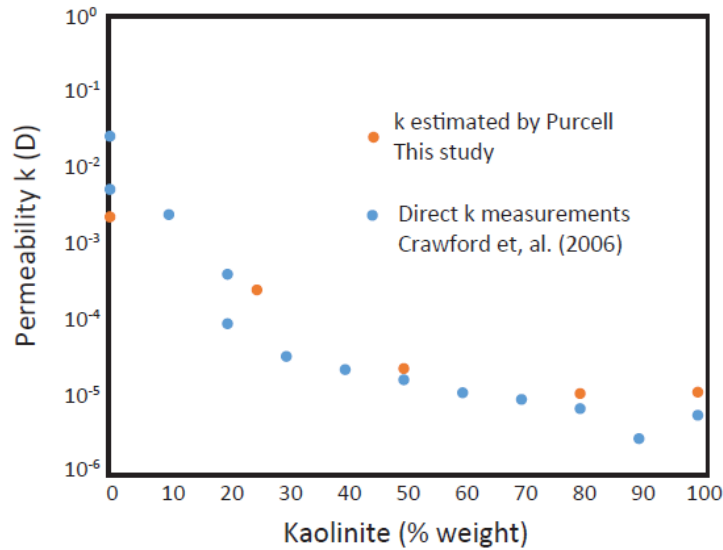
Figure 3.11: A comparison between permeability estimated by using Purcell's theory to permeability from direct measurements. Both sets of samples range from 100% quartz to 100% kaolinite. *Crawford et al.*, (2008) consolidated to 50 MPa and used water for their high permeability measurements and argon gas for their low permeability measurements.

Yang and Aplin (2010) developed an empirical relationship between void ratio and permeability based on 376 data points in the literature comprising natural and resedimented mudstones based on the fractional content of grains less than 2 microns and the total void ratio e (Eq. 4 in cited reference). The equation is empirical and heavily parametrized but has a coefficient of regression (r^2) equal to 0.93 and is thus a useful way of comparing our data to the larger literature. Applying this equation to our data, we find that it agrees within

an order of magnitude to our permeability estimates from MICP data using the Purcell model (Figure 3.12a).   In our Purcell model we used the smallest lithology factor used by Purcell; however, given the fine grained nature of our samples a smaller lithology factor could be justified.   The greatest disagreement between the MICP-Purcell estimates and those derived using Yang and Aplin (2010) occurs for the 100% quartz sample which is to be expected as their equation was originally fit only to fine grained mudrocks. Overall, we find that MICP permeability with Purcell's method agrees relatively well with mudrock permeability in the literature.
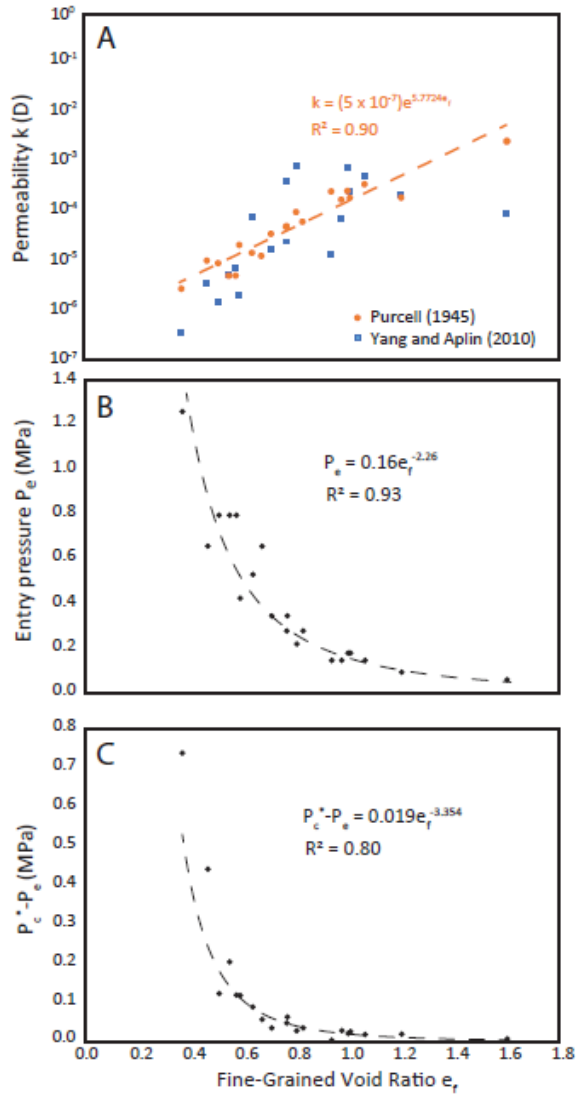
Figure 3.12: (A) Estimated permeability using the Yang and Aplin (2010) model and MICP results analyzed with the Purcell (1949) model, (B) entry pressure, and (C) breakthrough pressure-entry pressure difference all plotted as a function of fine-grained void ratio. The regression in (A) is for the permeability estimates using the MICP results.

Entry pressure and breakthrough pressure: Uncertainty in the contact angle of mercury with minerals adds uncertainty to entry and breakthrough pressure values.

Experiments have found the contact angle between mercury and air on kaolinite is 160° (*Penumadu and Dean*, 2000). However, the wettability of kaolinite is difficult to constrain due to the possibility that it contains both a water wet surface and a non-water wet surface (*Šolc et al.*, 2011). Like P_c^*, P_e is power law correlated with e_f (Figure 3.12b). This behavior can also be understood by the clogging of larger pores along the perimeter of the sample with fine grains. The difference between P_c^* and P_e increases with decreasing e_f (Figure 3.12c) which is to be expected given their respective power law relationships. Fundamentally, this spread represents the increase in non-wetting phase saturation needed to reach the breakthrough pressure. The greatest difference in P_c^* and P_e was observed in our pure kaolinite sample which had a non-wetting phase saturation of 0.31 at P_c^*. The smallest difference was observed in the 75% quartz/25% Kaolinite sample which had a non-wetting phase saturation of 0.06 at P_c^*. These MICP capillary entry and breakthrough pressure values (from 0.06 to 2 MPa) are in good agreement with those reported previously with direct pressure breakthrough measurements for scCO$_2$ in silty and clay-rich mudrocks ranging from 0.04 to 1.3 MPa (Espinoza and Santamarina, 2017).
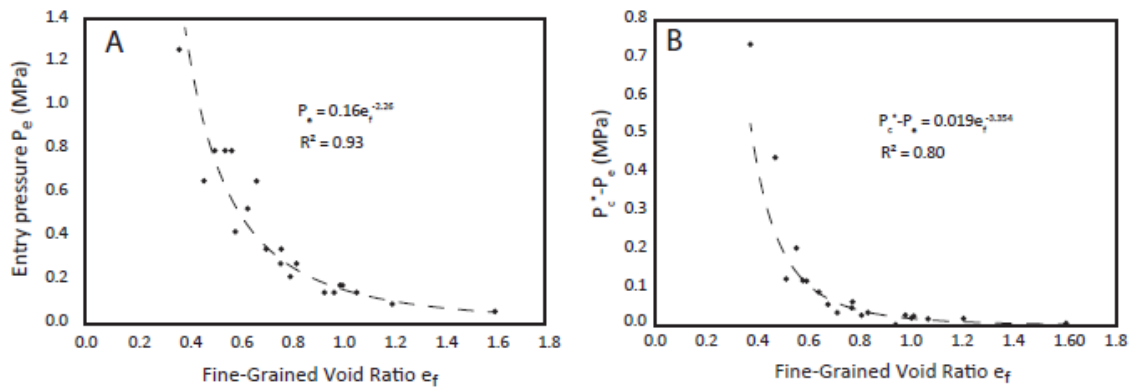
Figure 3.13: (A) Entry pressure as a function of fine-grained void ratio. B) The difference between percolation threshold and entry pressure.

55

3.5.4. Implications on Caprock Sealing Capacity

Inserting the breakthrough pressures measured in our experiments into Equation 3.1 we can predict the height of a CO_2 plume at the onset of percolation across a mudstone caprock for the entire range of sediment mixtures used in our study. At 13.8 MPa (2,000 psi) and 60° C, ρ_{CO2} is approximately 600 kg/m^3 (*Nordbotten et al.*, 2005) and for simplicity ρ_b can be estimated as 1000 kg/m^3. Hence, the expected CO_2 plume height would range from 16.4 m in our pure quartz silty sample to as much as 509 m in the pure kaolinite sample. The large variability of results highlights the impact of mudrock heterogeneity on potential mudrock sealing capacity. Ultimately the buoyant flow of CO_2 in the subsurface is controlled by the heterogeneity of the reservoir lithology including the bedding and facies distribution that compose the reservoir and caprock. Each of the samples in this study can be characterized with a single e_f. In reality, the e_f of a caprock will vary across the formation. Understanding this distribution is critical to predicting caprock integrity. Invasion-percolation modeling is often used to model this long-term buoyant fluid flow behavior due to its ability to include heterogeneity and its computational efficiency (*Trevisan et al.*, 2017). However, applying experimental entry pressures during modeling efforts may not be sufficient to predict CO_2 flow as seen at Sleipner (*Cavanagh and Haszeldine*, 2014). In addition to sediment deposition architecture, a detailed understanding of the lithology and an understanding of how $P_c{}^*$ scales with e_f will yield better prediction of the plume geometry at the basin scale.

Caprock wettability may be as important as caprock pore structure for determining sealing capacity. In this study we have assumed completely water-wet caprock ($\theta_{b/CO2} = 0°$). However, there is evidence of contact angles greater than 40° in quartz and clay minerals and even greater than 90° in organic matter-rich mudrocks (*Arif et al.*, 2017; *Chaudhary et al.*, 2015; *Espinoza and Santamarina*, 2010; *Guiltinan et al.*, 2017; *Iglauer*

et al., 2015; *Roshan et al.*, 2016). A CO_2-wet caprock may favor CO_2 storage within the caprock itself but could lead to leaks in the long term if the storage capacity is surpassed.

3.6 CONCLUSIONS

We resedimented samples composed of fine grained quartz, kaolinite, and lime. The addition of lime is shown to be an effective method for cementing resedimented samples. MICP analysis shows that the breakthrough pressure of these samples is correlated to the fine grained void ratio when the fine grains are taken to be those grains less than approximately 10 μm. We hypothesize that the 10 μm threshold for these samples correlates to the pore body and pore throats of the connected pathway at the percolation threshold. This means that the coarse grains control the structure of the percolating network while the void ratio within that network controls the transport properties. The simplicity of the power law relationship we observe between P_c^* and e_f is ideal because estimates of these parameters can be made using geophysical techniques, such as gamma and neutron logs. Permeability estimates of our samples compare well with literature data and we show that the *Yang and Aplin* (2010) empirical relationship based upon clay fraction and void ratio validates the results of our MICP-Purcell estimation. Our results are applicable to mudrocks that have undergone limited diagenesis and may not apply to shales where the percolating pore network can be filled with authigenic minerals. While the heterogeneity of natural mudrocks makes them difficult to systematically study, future work following our approach could be done to investigate if these relationships persists.

3.7 ACKNOWLEDGMENTS

Chapter 4: Multiphase fluid flow properties of rough fractures with heterogeneous wettability: analysis with lattice Boltzmann simulations

4.1 ABSTRACT

Fractures serve as preferential conduits for fluid flow in geological formations with low permeability. The transport properties of fractures are important in natural processes and in engineering applications such as the evaluation of sealing capacity of caprocks and hydrocarbon-bearing source rocks. Transport and flow in fractures are usually studied by investigating fracture aperture, roughness, and compressibility among other factors. However, most studies disregard wettability of the fracture surfaces and its influence on small-scale phenomena and effective properties. Here we use the lattice Boltzmann method to simulate and understand the displacement of water by supercritical CO_2 in synthetic fractures based on natural analogs with mixed wetting distribution. The heterogeneity of wetting properties significantly affects fracture multiphase fluid flow properties. We observe that heterogeneous wetting distributions including CO_2-wet surfaces promote the residual trapping of water and increase the CO_2 permeability compared to a completely water-wet case. Similarly to porous media, wetting heterogeneity increases CO_2 breakthrough time and sweep efficiency compared to the water-wet case. These results highlight the importance of wetting distributions on the transport of fluids in fractures.

4.2 INTRODUCTION

Geologic sequestration of CO_2 is considered a viable option for the reduction of CO_2 emissions into the atmosphere [*Pacala and Socolow*, 2004]. The process involves capturing CO_2 at massive emission points and pumping it into underground reservoirs where CO_2 rises buoyantly until trapped beneath a competent, low permeability caprock

such as an evaporite or shale rock [*Benson et al.*, 2005]. However, these formations, particularly brittle shales, may be fractured and thus may have high permeability pathways for buoyant fluids into overlying formations. Understanding the transport of CO_2 through fractures is critical for predicting CO_2 storage security, and potential leak rates.

The flow of two immiscible fluids through a fracture is controlled by the fracture geometry, fluid properties, wettability, and flow rates and pressure gradient [*Renshaw*, 1995; *Vogler et al.*, 2018; *Wang and Cardenas*, 2014; *Wang et al.*, 2015]. Due to the difficulty in conducting controlled experiments and computational challenges the effects of surface wetting properties are relatively unexplored. In porous media, it has long been understood that wettability impacts residual saturation and relative permeabilities.

The pore-scale controls on the transport properties of immiscible two-phase flow has been well studied [*Al-Raoush*, 2009; *Armstrong et al.*, 2012; *Blunt et al.*, 2013; *Chaudhary et al.*, 2013; *Culligan et al.*, 2006; *Dou et al.*, 2013; *Hao and Cheng*, 2010; *Hu et al.*, 2017]. Generally, investigating pore-scale systems requires solving the Navier-Stokes equations; however, this is computationally expensive and traditional methods struggle to incorporate the intermolecular forces responsible for wettability [*Chen and Doolen*, 1998; *Coon et al.*, 2014]. These forces are primarily due to Van Der Waals forces and hydrogen bonding and give rise to surface phenomena such as wettability, solubility, phase separation, and capillary pressure. The Lattice Boltzmann method allows for the inclusion of these forces in a simple manner while also solving the Navier-Stokes equations [*Aidun and Clausen*, 2010; *Chen and Doolen*, 1998; *Nourgaliev et al.*, 2003; *Zhang*, 2011].

The Lattice Boltzmann method (LBM) is based upon tracking a distribution of particles, $f_i(\mathbf{x}, t)$, moving upon a grid as they relax toward an equilibrium Boltzmann distribution f_i^{eq}. Intermolecular forces, both between fluids and walls, are easily incorporated through the application of an attractive or repulsive force on the particles

[*Chen and Doolen*, 1998]. In this way the LBM interparticle forces represent a more natural expression of intermolecular forces than traditional computational fluid dynamics (CFD) techniques. Recently *Zhao et al.* [2018] explored the effect of wettability heterogeneity on relative permeability of immiscible flow in porous media using LBM. They found that for water saturations between 0.3 -0.7 the relative permeability of random wetting distributions was less than that of purely water-wet or purely non-water wet, but that this reversed at very high or low saturations.

LBM has also been used to investigate fractures [*Dou et al.*, 2013; *Eker and Akin*, 2006; *Ju et al.*, 2017; *Kim et al.*, 2003; *Landry et al.*, 2014]. *Landry et al.* [2014] showed that LBM was able to accurately reproduce the matrix fluid transfer in an oil-wet and water-wet sintered glass fracture as visualized with X-ray computed microtomography. However, they were not able to reproduce the irreducible water saturation and hypothesized that a significantly finer resolution may be needed. *Dou et al.* [2013] investigated the effect of altering the magnitude of wetting in a homogenously wet self-affine fracture. Due to their homogenous wetting conditions the flow field in each fracture was similar but the wettability magnitude had a significant effect on the evolution of effective interfacial area in time.

In this study we seek to investigate the effect of a non-uniform wettability distribution on CO_2 flow in fractures through the use of the "explicit-forcing" (EF) multicomponent Shan and Chen model proposed by *Porter et al.* [2012]; [*Shan and Chen*, 1993; 1994]. We apply wetting parameters informed by real world shale mineral distributions to a single synthetic fracture and explore their effect on unsteady state relative permeability and the evolution of the CO_2 flow. Finally, we explore the effect of wetting magnitude on residual saturation.

4.3 METHODS

4.3.1. Lattice Boltzmann Method and the Taxila Code

Taxila LBM is an open source LBM code developed at Los Alamos National Laboratory [*Coon et al.*, 2014; *Porter et al.*, 2012] (https://github.com/ecoon/Taxila-LBM). Taxila implements the multicomponent interparticle-potential model known as the Shan-Chen (SC) model [*Shan and Chen*, 1993; 1994] as outlined in *Porter et al.* [2012]. The SC model is one of the most popular LB implementations, yet drawbacks such as large spurious currents near interfaces, viscosity-dependent equilibrium densities, and numerical instabilities for large density and kinematic viscosity ratios have prevented this model from accurately investigating many multiphase systems. The explicit forcing (EF) model which was first proposed by *Yu et al.* [2011] and extended by *Porter et al.* [2012] helps address these issues. The model allows for viscosity-independent equilibrium densities and is capable of simulating kinematic viscosities greater than 1,000 with reduced spurious currents at fluid-fluid interfaces [*Porter et al.*, 2012].

The lattice Boltzmann method involves solving the discrete Boltzmann equation for a distribution of particles moving on a discrete grid of sites x at time t with fixed velocities, e_i, where i represents each of the fixed velocity directions. The particle distribution is described by the function f_i ($\mathbf{x}$, e_i, t). In our model we use the three dimensional D3Q19 model which contains 19 possible fluid velocity directions, 18 to neighboring lattice sites and 1 stationary velocity [*Chen and Doolen*, 1998]. If each particle at x travels at velocity e_i they will arrive at a new position according to

$$f_i^k(x + e_i\Delta t, e_i, t + \Delta t) = f_i^k(x, e_i, t) \qquad (4.1)$$

62

where *k* represents the *k*th fluid component (2, in our case). However, if during the process of travelling each particle is subject to collisions and outside forces equation 1 becomes

$$f_i^k(\boldsymbol{x} + \boldsymbol{e}_i \Delta t, \boldsymbol{e}_i, t + \Delta t) - f_i^k(\boldsymbol{x}, \boldsymbol{e}_i, t) = \Omega_{coll}^k + \Omega_{forces}^k \tag{4.2}$$

This is known as the discrete Boltzmann equation, where Ω_{coll}^k represents momentum changes to the particle distribution from particle collisions and Ω_{forces}^k represents momentum changes due to other forces. The left hand side of this equation is known as the "streaming step" and the right hand said is the "collision step". In the SC model external forces are incorporated through a momentum adjustment into the equilibrium velocity [*Shan and Chen*, 1993], thus there is no Ω_{forces}^k, however in the EF model this forcing term is directly included in the Boltzmann equation. The collision operator is defined as

$$\Omega_{coll}^k = \boldsymbol{\Lambda}^k [f_i^{eq,k}(\boldsymbol{x}, t) - f_i^k(\boldsymbol{x}, t)] \tag{4.3}$$

where $\boldsymbol{\Lambda}^k$ is the relaxation operator and $f_i^{eq,k}$ is the equilibrium distribution function

$$f_i^{eq,k} = \omega_i \rho_i [1 + \frac{\boldsymbol{e}_i \cdot \boldsymbol{u}^{eq}}{c_s^2} + \frac{(\boldsymbol{e}_i \cdot \boldsymbol{u}^{eq})^2}{c_s^2} + \frac{\boldsymbol{u}^{eq} + \boldsymbol{u}^{eq}}{c_s^2}] \tag{4.4}$$

where ω_i represents the weights to the velocity components which, for a D3Q19 lattice are $\omega_0 = 1/3$, $\omega_1 = 1/18$, $\omega_{\sqrt{2}} = 1/36$, and $\omega_{\sqrt{3}} = 0$ according to *Aidun and Clausen* [2010] and $\boldsymbol{u}^{eq}$ is an effective velocity. Equation 4 comes from matching macroscopic dynamics using a Chapman-Enskog expansion and has been shown to correspond to the second-order Hermite expansion [*Porter et al.*, 2012]. The forces operating on the particles are given by

63

$$\Omega_{forces}^k = \frac{\Delta t}{2} [f_i^{F,k}(x + e_i \Delta t, t + \Delta t) + f_i^{F,k}(x, t)] \tag{4.5}$$

where

$$f_i^{F,k} = \frac{F^k \cdot (e_i - u^{eq})}{\rho_k c_s^2} f_i^{eq,k} \tag{4.6}$$

F^k is a vector of forces, ρ_k is the density and c_s is the speed of sound on the lattice which is $\frac{1}{\sqrt{3}}$ on the D3Q19 lattice. The intermolecular forces are incorporated into F^k. The wettability forces are given by

$$F^k = -\rho_k(x) \sum_{m=1}^{n_m} g_k^m \sum_{x' \in W_m} (x' - x) \tag{4.7}$$

where g_k^m represents the intermolecular forces between the fluid, k, and mineral m. W_m represents the set of neighboring wall nodes that are composed of mineral m. Due to the negative sign, positive g_k^m forces represent non-wetting forces. The interparticle forces which give rise to interfacial tension can be included in a similar nearest neighbor manner, however, it has been shown that longer range interparticle forces help reduce spurious currents and increase numerical stability [*Shan*, 2006]. These forces are incorporated as

$$F^k(x) = -\psi_k(x) \sum_{k=1}^{n_k} \sum_{x' \in N_x} G_{k,\bar{k}}(x' - x) \frac{\psi_{\bar{k}}(x') - \psi_{\bar{k}}(x)}{|x' - x|} (x' - x) \tag{4.8}$$

Where $\psi_k(x)$ is the effective mass. N_x are the lattice sites that are not walls and whose direct path from x to x' do not include walls. $G_{k,\bar{k}}$ is a Greens function which is 0 at distances greater than the desired range of interparticle forces and is $g_{k,\bar{k}}\hat{G}$ when within range. $\hat{G}$ enforces isotropy according to *Shan* [2006] and $g_{k,\bar{k}}$ indicates the magnitude of

the force. In our models, 8 orders of isotropy were enforced. Taxila also allows for the implementation of multiple relaxation times which allow for varied viscosity ratios. More details regarding Taxila are available elsewhere [*Porter et al.,* 2012].

4.3.2 Synthetic Fracture Generation and Model Geometry

We used SynFrac, a program developed to create synthetic fractures based on natural analogs [*Ogilvie et al.*, 2006]. A 128 x 128 pixel fracture was created using the Brown method with a standard deviation of 5, a mismatch length of 45, and a fractal dimension of 1. The fracture was repeated once in the y-direction to create a fracture that was 128 x 256. The average aperture is 6.7 voxels (lu) with a minimum of 2 and maximum of 14 voxels (Figure 4.1a). The final 6 rows were repeated in the y-direction for stability concerns at the outlet.
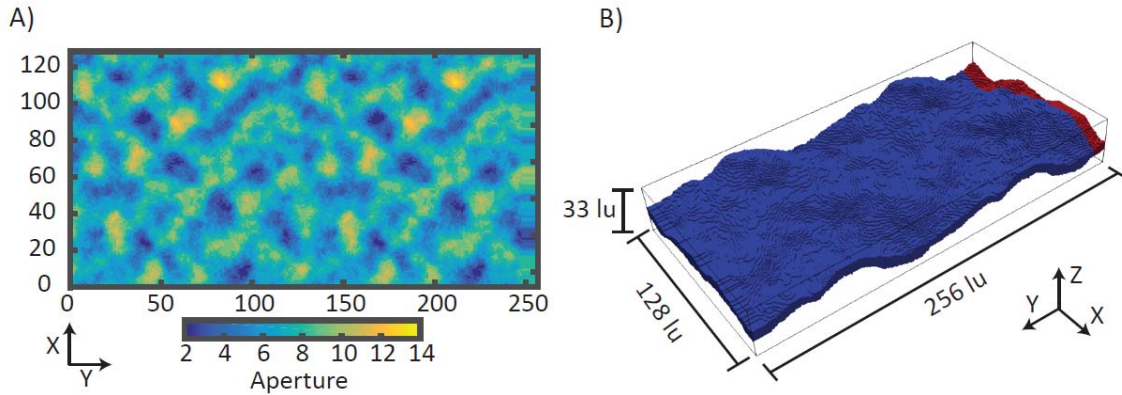
Figure 4.1: A) Fracture aperture map. The aperture ranges from 2 lu to 14 lu with an average aperture opening of 6.7 lu. The final 6 rows at the outlet are repeated for stability reasons. B) The model domain is 128 x 256 x 33 lu with a constant pressure inlet at y =0 and a constant pressure outlet at y = 256.

To convert our lattice units into physical properties we assume the average aperture opening corresponds to a fracture opening of 50 μm, this results in a dx of 7.46 μm.

Apertures of 50 μm are commonly observed in the Barnett formation [*Gale et al.*, 2007]. In order to recover the Navier-Stokes solution, the LBM assumes incompressible flow. This assumption is only valid when the lattice velocity is significantly less than the speed of sound on the lattice, otherwise known as a low Mach number. To remain in the incompressible regime we assume the convention of dt/dx = 0.01 which provides us with a time step of 7.5×10^{-8} seconds. We use dt and dx to convert our units to physical properties, however the dimensionless solutions of LBM and the Navier-Stokes equations mean our results could also be applied to fractures of different apertures.

The model domain is 128 x 256 x 33 lu and is initialized with CO_2 present in the first 10 columns along the y-axis while water defends in the remaining fracture (Figure 4.1b). CO_2 invades the fracture at a constant pressure inlet at y = 0 and both fluids are allowed to exit the outlet at y = 256. The inlet pressure in lattice units is 0.38 and the outlet is 0.33 which corresponds to a differential pressure of 500 Pa in physical units. The model is periodic in the x direction.

4.3.3 Heterogenous Wettability Distributions

Wettability distributions were informed by actual mineral distributions in an organic shale using the images presented by *Gerke et al.* [2015]. *Gerke et al.* [2015], developed a method for fusing multiscale images obtained from x-ray microtomography and scanning electron microscopy into one image. They demonstrated their technique on a organic shale from the Bazhenov formation in Siberia where they created an image with four components with distinct wetting properties: macroscale minerals, a mixture of minerals and kerogen, resolved kerogen, and kerogen nano-porosity. We sub-sampled their image (*Gerke et al.,* 2015, supplemental information Figure SI.7c) into a 744 x 372

image and created three new images which contain similar histograms but different mineral distributions (Figure 4.2, 4.3a). The correlation length of the minerals (light blue phase) increases from mineral distribution A through C with the original image being the most correlated (Figure 4.3b). These distributions were then draped onto the fracture walls in our model. Along with the four heterogeneous wetting distributions we also explored the effect of a completely nonwetting and a completely wetting case.
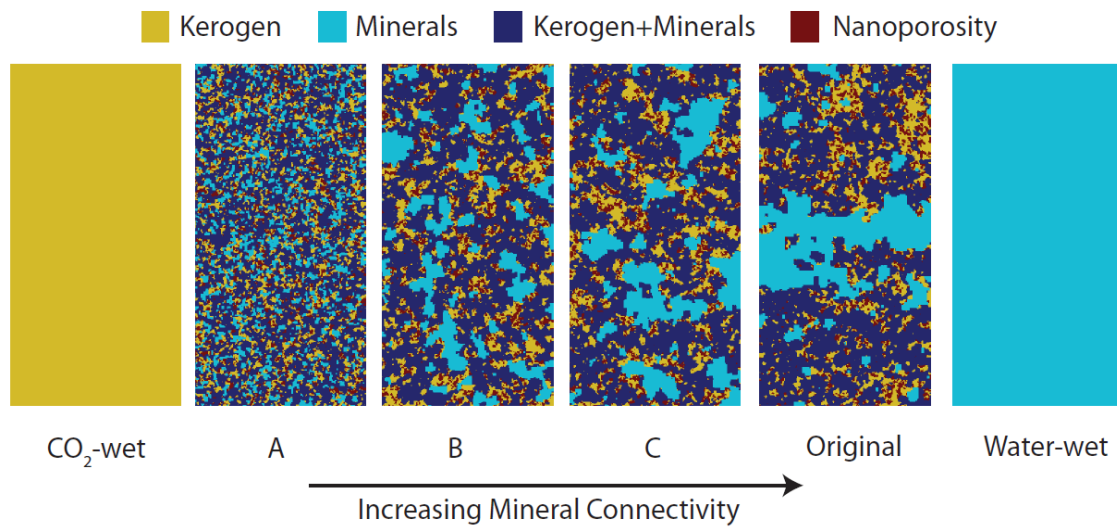
Figure 4.2. Five different wetting distributions applied to the fracture walls. Colors represent different phases: orange - kerogen, red - kerogen nanoporosity, dark blue - mixture of kerogen and minerals, and light blue - mineral. Original image from *Gerke et al.*, 2015.
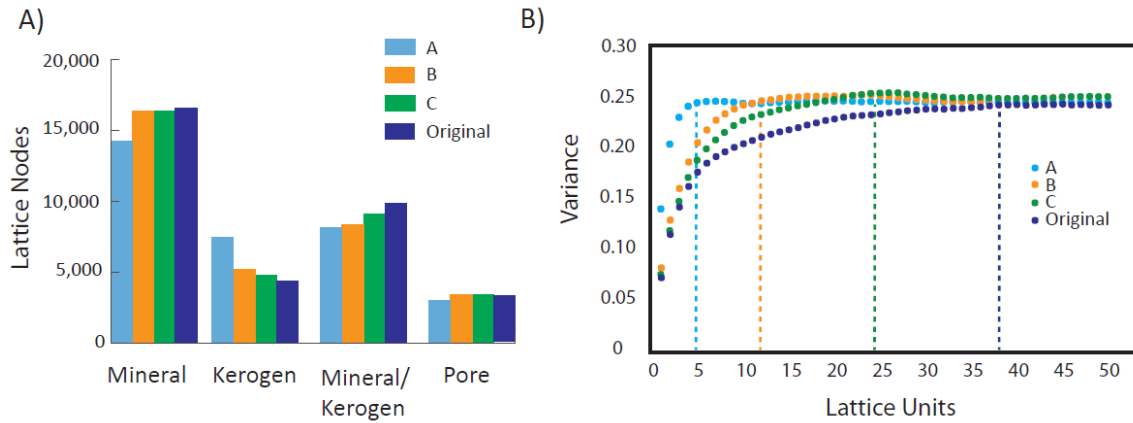
Figure 4.3: A) Histogram of the mineral components in each wetting distribution. B) Variograms of the mineral component of each wetting distribution. The correlation length of wetting distributions A, B, C, and the original image are approximately 5, 11, 24, and 376 lattice units respectively.

4.3.4 Parameter Tuning

The lattice wettability force, g_k^m, between CO_2 and each mineral pair in our model was 0.09 for minerals, 0.045 for minerals and kerogen, 0 for kerogen nano-porosity, and -0.09 for kerogen. For water the values were reversed. Capillary models were conducted to measure the resultant contact angles due to these forces (Figure 4.4a). The interparticle force, $g_{k,\bar{k}}$, was set to 0.21. This value was found to maximize immiscibility while maintaining numerically stability. The EF model has been shown to reproduce the Laplace equation [*Porter et al.*, 2012] and so the pressure differential inside and outside of a bubble was used to calculate the interfacial tension (Figure 4.4b). Under these conditions, σ = 0.1785 in lattice units and the capillary number for our models is 8×10^{-4}. Fluid flows at capillary numbers below approximately 1×10^{-5} are dominated by capillary force [*Peters*, 2012]. Our capillary number chosen can be considered a transitional capillary number; the flow is viscous but also influenced by capillary forces. In a CO_2 security perspective, flow through a fracture will occur once the initial breakthrough pressure is reached and which

68

should occur at low capillary number; however, in engineered systems such as CO_2 flooding in a hydrocarbon reservoir the capillary number will likely be much higher.
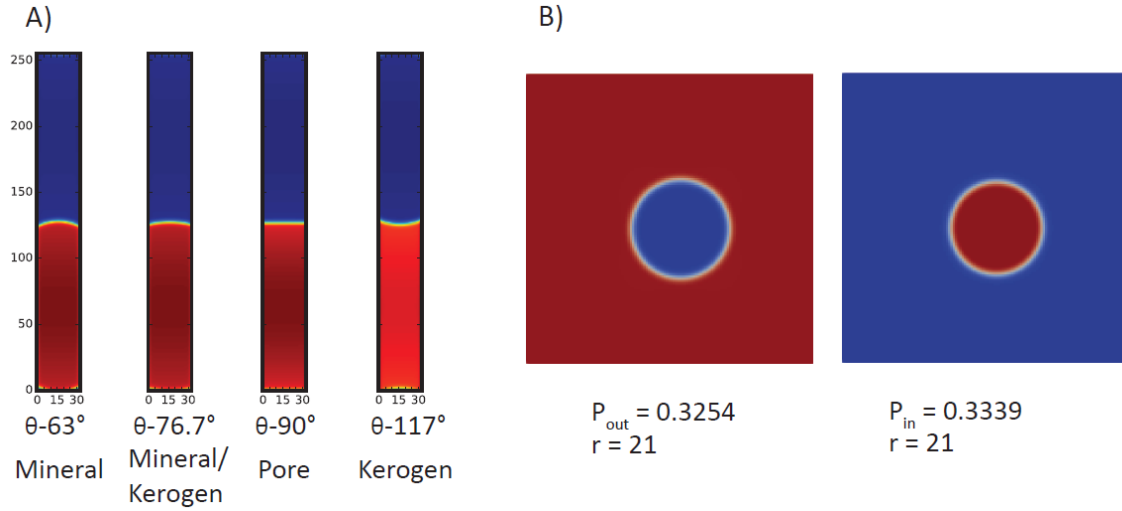
Figure 4.4. A) Contact angles for each mineral identified in *Gerke et al.,* 2015. B) IFT between fluids is calculated as σ =dP*r. σ -0.1785

The Lattice Boltzmann method is a finite difference scheme and thus the resolution of the model can impact the accuracy of the flow field. Given sufficiently large fractures LBM has been shown to accurately reproduce the analytical solution for flow between parallel plates, an analog for fractures [*Ju et al.*, 2017; *Kim et al.*, 2003]. However, our fracture, with lattice nodes as narrow as 2 lu is designed mimic a real world fracture where the aperture will occasionally reach zero as the fracture walls contact each other. To investigate the accuracy of the Taxila LBM code in areas where the aperture becomes very small we conducted a series of two dimensional parallel plate models using the same model parameters as our larger 3D fracture (Figure 4.5). The parallel plate models range from a fracture width of 1 lu to 6 lu. Resolution errors increase as the as the aperture decreases but remain very accurate down to approximately 4 lu. The area of our fracture that is

composed of apertures of two and three lu is only 1.0 and 3.7 percent respectively. By volume, these apertures compose only 0.3 and 1.7 percent of the fracture respectively and therefore these errors are assumed to be negligible.
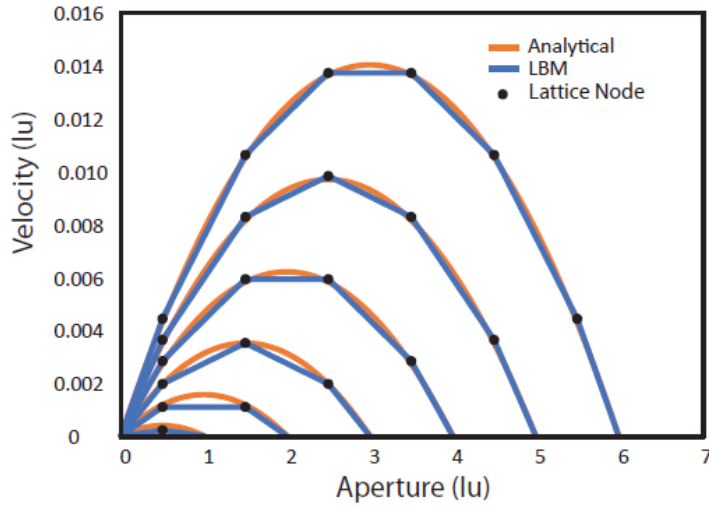
Figure 4.5. Comparison between simulations of flow between parallel plates and the analytical solution.

4.4 RESULTS AND DISCUSSION

4.4.1 CO_2 plume evolution and residual trapping

The CO_2 plume evolution is controlled by both the fracture aperture and the wettability distribution (Figure 4.6).
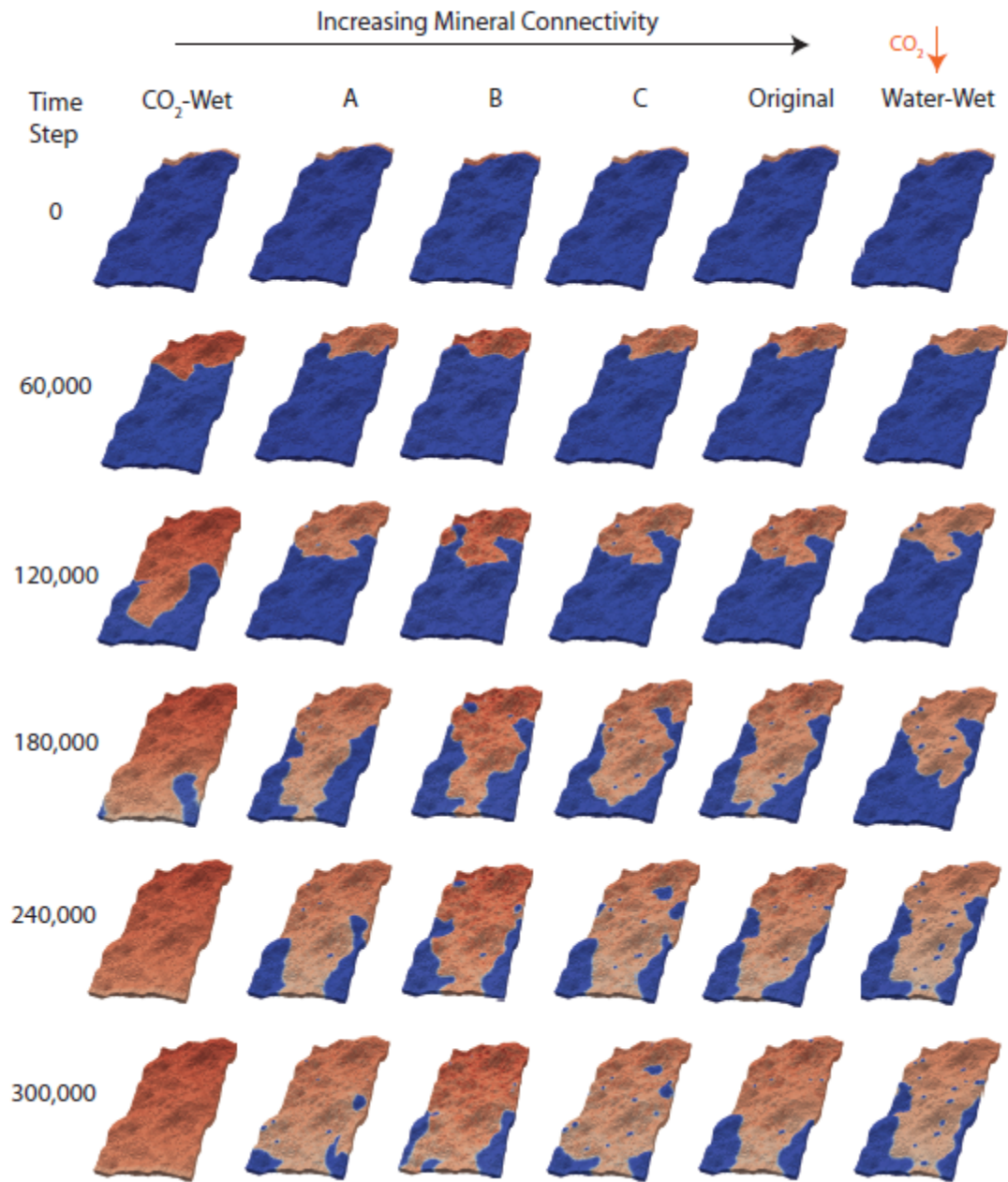
Figure 4.6. Evolution of CO₂ plume during each model run. In general, the CO₂ reaches the outlet sooner, leaves less residual saturation, and provides greater sweep efficiency when the water wet minerals are less connected.

The completely CO_2 wetting and completely water-wetting cases bound the behavior of the system with the heterogeneous wetting cases falling in between. In general, as the water- wet mineral connectivity is increased, time to breakthrough is increased and the water sweep efficiency by CO_2 is reduced (Figure 4.7).
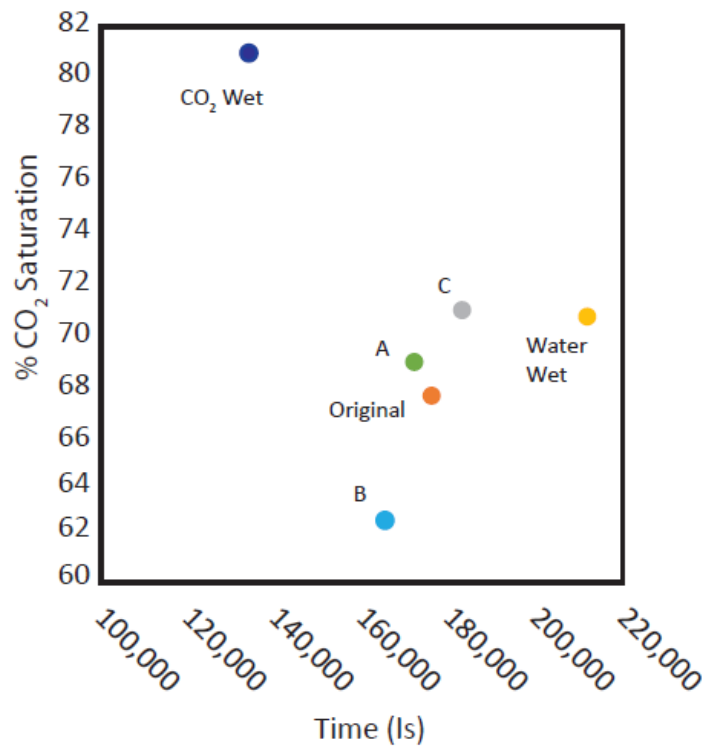
Figure 4.7: A) % CO_2 Saturation and dimensionless time step at breakthrough. The CO_2 non-wet fractures takes the longest to breakthrough. The CO_2 wet fracture has the highest CO_2 saturation and breaks through the quickest.

The completely water-wet case has many small residually trapped water pockets while the largest and most stable pockets are formed with the wetting distribution "C". The small residually trapped pockets are often thin films which reside on the upper or lower face of the fracture wall. The films are formed in small pits in the fracture wall. Other

small bubbles which extend from fracture wall to wall are formed where a narrow fracture aperture corresponds with a non CO_2-wet mineral. This phenomena was most prevalent in the completely water-wet case and was appropriately absent from the CO_2-wet case.

Interestingly, the larger residual pockets were not formed in the completely water-wet case. They are formed where a less water-wet or a CO_2-wet mineral provides a short-circuit around a stalled portion of the CO_2 front. This short circuit allows the CO_2 to bypass the water until it is completely encompassed. The completely water-wet did not exhibit this trapping method. The original wetting distribution did not trap large residual bubbles because the water-wet minerals were aligned completely across the sample. This distribution did not provide any pathway to be short circuited by the invading CO_2. This means that residual saturation was not effected simply by the proportion of the wetting and non-wetting minerals but also by its heterogeneous spatial distribution.

To explore this phenomenon further, the wetting distribution C was used for two additional models with the magnitude of the wetting force increased by 1.25x and 1.5x the original wetting force (Figure 4.8). The prevalence of large residually trapped pockets increased as the wetting magnitude increased. At 1.5x a steady state flow pattern was established with 19% residual water saturation.
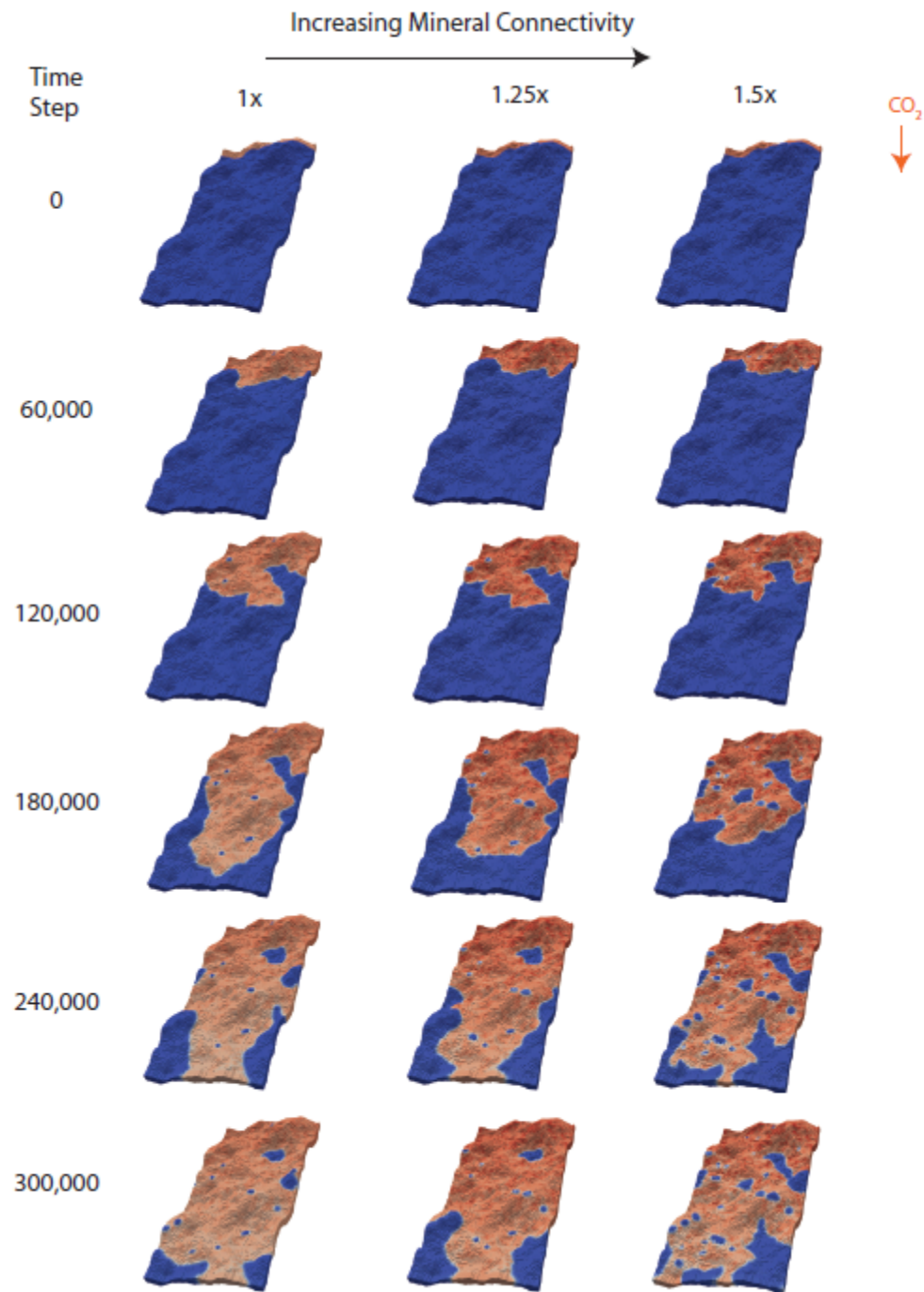
Figure 4.8: Evolution of CO₂ plume in fracture with mineral distribution C. Breakthrough time and sweep efficiency are reduced as the wetting magnitude is increased.

4.4.2 Unsteady Displacement

The displacement of water by CO_2 is an inherently dynamic process. The overall average flux of both phases at the outlet grows through time due to an increase in the saturation of CO_2. Initially, the production ratio which is the flux of water (q_w) divided by the total flux ($q_w + q_{C02}$) is 1 as the outlet produces pure water (Figure 4.9). Once breakthrough occurs the amount of CO_2 produced increases rapidly and the production ratio falls sharply. cases.
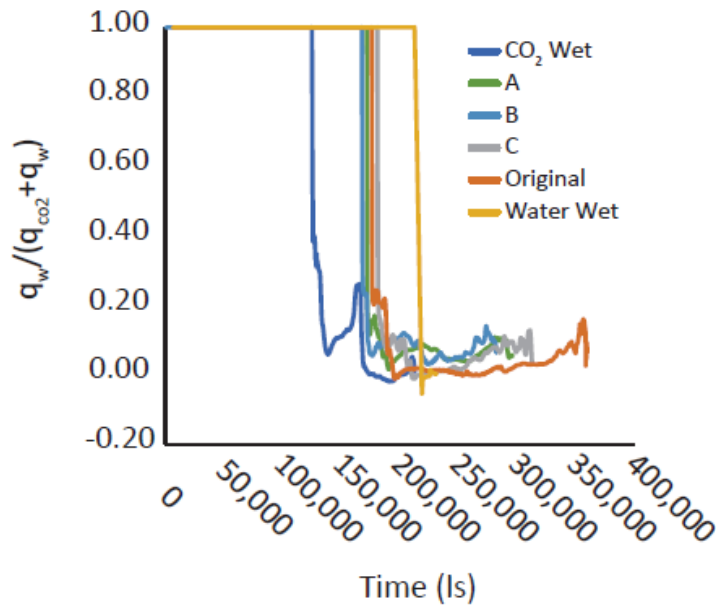
Figure 4.9. Water production ratio at outlet of fracture. Breakthrough time indicated by dramatic decrease in water production.

During CO_2 flooding at steady state the injected CO_2 volume is equal to the extracted CO_2 and no oil is produced. While relative permeability is typically measured at steady states, in reality it is the evolution of permeability through time that is important for engineering applications. Measuring unsteady state relative permeability is a dynamic process, where the pressure drop, *dp,* and length, *dl,* are time dependent. At high capillary

75

numbers and in homogenous medium, capillary forces can be assumed negligible and a sharp front can be formed [*Buckley and Leverett*, 1942]. Measuring unsteady relative permeability at lower capillary numbers and in the presence of strong wettability forces has many challenges. First, the capillary pressure scales along the CO_2 front with the wetting force and fracture aperture. Second, the absence of piston like displacement means the front must be estimated. One technique is to conduct experiments using gravity drainage and to neglect capillary pressure [*DiCarlo et al.*, 2000; *Kianinejad et al.*, 2016]. This technique can also be applied in the LBM by applying a body force to both fluids [*Hao and Cheng*, 2010; *Ramstad et al.*, 2012]. However, our models are meant to reflect the CO_2 displacement process.

To evaluate the unsteady permeability of our models, an interface detection algorithm was developed that measures the capillary pressure as well as the location of the interface with respect to the outlet. The algorithm avoids the low pressure environment caused by the spurious currents along the interface by advancing 7 lattice units away from either side of the interface. Observations of the interface show that after 7 lattice units the pressure field returned to normal. In this manner, hundreds of capillary pressure measurements of the interface and its location are made. Before breakthrough, these measurements were averaged which allowed for the estimation of unsteady CO_2 permeabilities (Figure 4.10). After breakthrough, the flux of CO_2 at the outlet and the pressure gradient across the entire fracture were used. The absolute permeability is shown at 100% CO_2 saturation and was developed with separate model runs of completely saturated fractures. These unsteady CO_2 permeability curves were generated using an average pressure gradient across the average length of the CO_2 plume with an average flux across the model. Despite this, the method provided meaningful results which trend towards the absolute permeability.
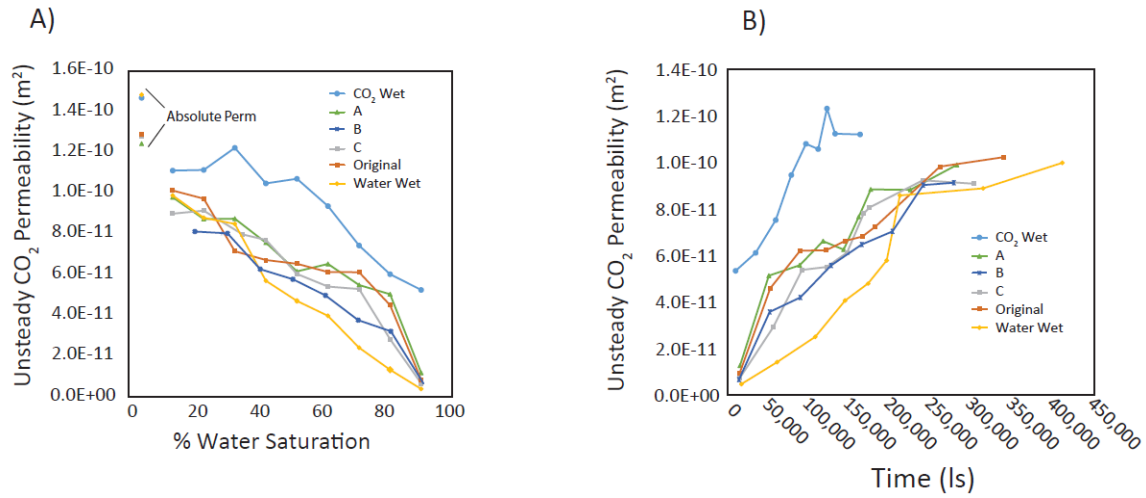
Figure 4.10. Unsteady CO₂ permeability of each fracture wetting distribution in terms of (A) % water saturation, and (B) non dimensional model time steps. Absolute permeabilities shown at 100% saturation in A are from a separate, fully saturated, model runs.

The unsteady CO_2 permeability evolution is similar to the total flux. It is generally bounded by the CO_2-wet and non CO_2-wet fracture. At higher saturations, the non-CO_2 wet fracture becomes more permeable than the heterogeneous fractures. This behavior is likely equivalent to non-wetting flow in porous media where the non-wetting phase occupies the largest pores and has a higher relative permeability compared to the wetting phase. At the same saturations, the CO_2 in the non CO_2-wet case occupies the largest fracture diameters. Interestingly, the heterogeneous wetting distributions have reduced absolute permeabilities compared to the CO_2-wet and non CO_2-wet fractures. Heterogeneous forces at the walls may be inducing more tortuous currents and increasing friction along the walls. This phenomenon should be explored further. Increasing the wetting forces in wetting distribution "C" appears to have little effect on the CO_2 permeability despite having significant effects on the residual trapping and distribution of the CO_2 plume. This means the areas of increased residual saturation were contributing

very little to the flux of CO_2 when occupied by CO_2. This suggests that it is the distribution of wetting parameters that controls the evolution of unsteady permeability more so than the magnitude of the wetting forces.
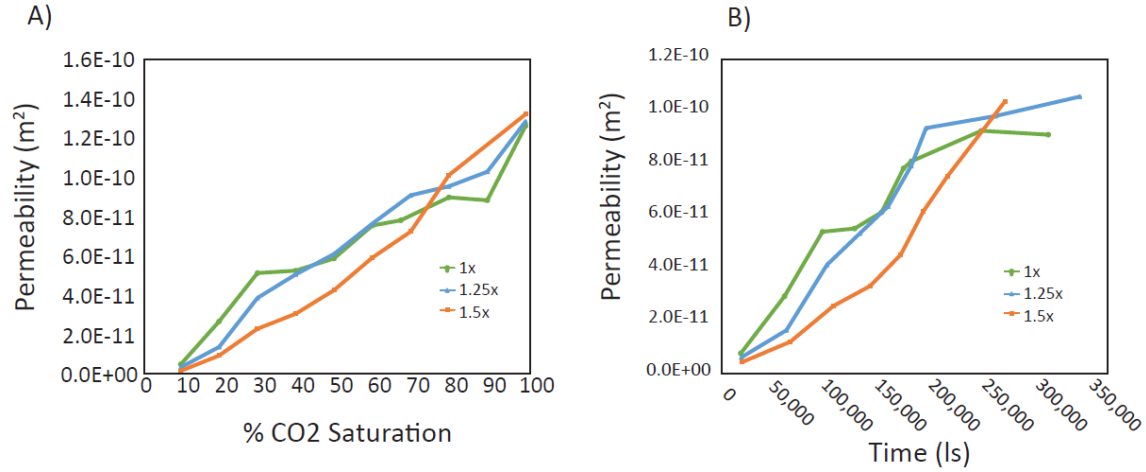
Figure 4.11. Effect of wetting strength on the evolution of unsteady CO_2 permeability in terms of (A) % CO_2 saturation, and (B) non dimensional model time steps. Absolute permeabilities shown at 100% saturation in A are from a separate, fully saturated, model runs.

4.5 CONCLUSIONS

We used the explicit forcing lattice Boltzmann model developed by *Porter et al.* [2012] to simulate CO_2 displacement of water in a fracture with heterogeneous wetting distributions informed from an organic shale. We observed short-circuiting of the CO_2 front caused by wetting distributions that promote residual saturations. Unsteady CO_2 permeabilities were estimated from the average capillary pressure along the front. The evolution of permeability varied significantly between completely CO_2-wet and non CO_2-wet fractures but little difference was observed between fractures with the same proportion of wetting properties but different distributions. Simulations on the same wetting distributions but with stronger wetting forces show that as the wetting strength increases

78

the residual trapping is also increased but the unsteady CO_2 permeability evolution is little changed. Future work is needed to explain absolute permeability differences between heterogeneous and homogeneous wetting distributions and to explore the effect of heterogeneous wetting distributions with stronger wetting parameters.

4.6 ACKNOWLEDGMENTS

Chapter 5: Summary

5.1 SUMMARY AND FUTURE WORK

Pore-scale scale properties influence core-scale to continuum scale multiphase fluid flow. This dissertation examines how these effects influence the caprock integrity during geologic CO_2 sequestration but the fundamentals apply to other multiphase systems.

In Chapter 2, I present the findings from wettability measurements at reservoir conditions on an organic shale. I demonstrated that the organic matter concentration and thermal maturity of organic shales is unlikely to cause them to be CO_2 wet. This is an important finding and means that the entry pressure of CO_2 into these caprocks may remain high. However, the wettability of non-organic and organic shales varies widely. This deserves further research to explain. It is possible that the mineralogy of the shales is exerting control over the wetting or that the history of the shales exposure to geologic fluids may override any mineralogical control. The fundamental controls on wettability in reservoirs are still poorly understood.

In Chapter 3, I use the resedimentation process to create synthetic mudstones with controlled mineralogies and known grain size distributions. Using mercury intrusion porosimetry I measure the entry pressure, and estimate the breakthrough pressure and permeability. As discussed, other researchers have shown the effect of void ratio on permeability of similar samples. I expand on this work and present a novel relationship between fine-grained void ratio and breakthrough pressure. I hypothesize that the fine-grained cut-off diameter is controlled by the structure of a larger coarse grained percolating pore network. Future work could investigate these parameters in natural shales, possibly through the use of FIB-SEM to identify the proportion of coarse and fine grains.

In Chapter 4, I present the results of lattice Boltzmann simulations on a fracture. For the first time, I investigate the role of heterogeneous wetting distributions on the evolution of the residual saturation and relative permeability. These models reveal how heterogeneity in the wetting field can result in short-circuiting of the predominately wetting phase and increase residual saturation. In these simulations we use only one fracture and due to computational constraints the geometry is poorly refined. This coarse grid causes small pockets, or films, of trapped brine at the fracture face. This may or may not be physically appropriate. With a more highly refined fracture the effects of roughness on these thin films could be explored. It is possible that the increase in permeability to the nonwetting phase may be due to these films naturally smoothening the flow field.

References

Adams, A. L., J. T. Germaine, P. B. Flemings, and R. J. Day-Stirrat (2013), Stress induced permeability anisotropy of Resedimented Boston Blue Clay, *Water Resources Research*, *49*(10), 6561-6571.

Aidun, C. K., and J. R. Clausen (2010), Lattice-Boltzmann Method for Complex Flows, *Annu. Rev. Fluid Mech.*, *42*(1), 439-472.

Akbarabadi, M., and M. Piri (2013), Relative permeability hysteresis and capillary trapping characteristics of supercritical CO_2/brine systems: An experimental study at reservoir conditions, *Advances in Water Resources*, *52*(0), 190-206.

Al-Raoush, R. I. (2009), Impact of Wettability on Pore-Scale Characteristics of Residual Nonaqueous Phase Liquids, *Environ. Sci. Technol.*, *43*(13), 4796-4801.

Al-Yaseri, A. Z., H. Roshan, M. Lebedev, A. Barifcani, and S. Iglauer (2016), Dependence of quartz wettability on fluid density: Fluid Density-Quartz Wettability, *Geophysical Research Letters*, *43*(8), 3771-3776.

Allam, R., S. Martin, B. Forrest, J. Fetvedt, X. Lu, D. Freed, G. W. Brown Jr, T. Sasaki, M. Itoh, and J. Manning (2017), Demonstration of the Allam Cycle: an update on the development status of a high efficiency supercritical carbon dioxide power process employing full carbon capture, *Energy Procedia*, *114*, 5948-5966.

Arif, M., M. Lebedev, A. Barifcani, and S. Iglauer (2017), Influence of shale-total organic content on CO_2 geo-storage potential, *Geophysical Research Letters*, *44*(17), 8769-8775.

Armstrong, R. T., M. L. Porter, and D. Wildenschild (2012), Linking pore-scale interfacial curvature to column-scale capillary pressure, *Advances in Water Resources*, *46*, 55-62.

Arts, R., O. Eiken, A. Chadwick, P. Zweigel, L. van der Meer, and B. Zinszner (2004), Monitoring of CO_2 injected at Sleipner using time-lapse seismic data, *Energy*, *29*(9), 1383-1392.

Bachu, S., and D. B. Bennion (2009), Interfacial Tension between CO_2, Freshwater, and Brine in the Range of Pressure from (2 to 27) MPa, Temperature from (20 to 125) degrees C, and Water Salinity from (0 to 334 000) mg(.)L(-1), *Journal of Chemical and Engineering Data*, *54*(3), 765-775.

Bandini, P., and S. Sathiskumar (2009), Effects of Silt Content and Void Ratio on the Saturated Hydraulic Conductivity and Compressibility of Sand-Silt Mixtures, *Journal of Geotechnical and Geoenvironmental Engineering*, *135*(12), 1976-1980.

Benson, S., P. Cook, J. Anderson, S. Bachu, H. Nimir, B. Basu, J. Bradshaw, G. Deguchi, J. Gale, and G. von Goerne (2005), Underground geological storage, *IPCC special report on carbon dioxide capture and storage*, 195-276.

Benson, S. M., and T. Surles (2006), Carbon dioxide capture and storage: An overview with emphasis on capture and storage in deep geological formations, *Proceedings of the Ieee*, *94*(10), 1795-1805.

Bikkina, P. K. (2011), Contact angle measurements of CO_2–water–quartz/calcite systems in the perspective of carbon sequestration, *International Journal of Greenhouse Gas Control*, *5*(5), 1259-1271.

Blunt, M. J., B. Bijeljic, H. Dong, O. Gharbi, S. Iglauer, P. Mostaghimi, A. Paluszny, and C. Pentland (2013), Pore-scale imaging and modelling, *Advances in Water Resources*, *51*(0), 197-216.

Bohloli, B., E. Skurtveit, L. Grande, G. O. Titlestad, M. H. Børresen, Ø. Johnsen, and A. Braathen (2014), Evaluation of reservoir and cap-rock integrity for the Longyearbyen CO_2 storage pilot based on laboratory experiments and injection tests, *Norwegian Journal of Geology / Norsk Geologisk Forening*, *94*(2/3), 171-187.

Borysenko, A., B. Clennell, R. Sedev, I. Burgar, J. Ralston, M. Raven, D. Dewhurst, and K. Liu (2009), Experimental investigations of the wettability of clays and shales, *Journal of Geophysical Research: Solid Earth*, *114*(B7), B07202.

Botto, J., S. J. Fuchs, B. W. Fouke, A. F. Clarens, J. T. Freiburg, P. M. Berger, and C. J. Werth (2017), Effects of Mineral Surface Properties on Supercritical CO_2 Wettability in a Siliciclastic Reservoir, *Energy & Fuels*, *31*(5), 5275-5285.

Broseta, D., N. Tonnet, and V. Shah (2012), Are rocks still water-wet in the presence of dense CO_2 or H2S?, *Geofluids*, *12*(4).

Brown, A. A. (2015), Interpreting Permeability from Mercury Injection Capillary Pressure Data, *AAPG 2015 Annual Convention and Exhibition, Denver, Colorado, May 31-June 3*.

Buckley, S. E., and M. C. Leverett (1942), Mechanism of Fluid Displacement in Sands.

Busch, A., P. Bertier, Y. Gensterblum, G. Rother, C. J. Spiers, M. Zhang, and H. M. Wentinck (2016), On sorption and swelling of CO_2 in clays, *Geomechanics and Geophysics for Geo-Energy and Geo-Resources*, *2*(2), 111-130.

Cassie, A. B. D., and S. Baxter (1944), Wettability of porous surfaces, *Transactions of the Faraday Society*, *40*(0), 546-551.

Cavanagh, A. J., and R. S. Haszeldine (2014), The Sleipner storage site: Capillary flow modeling of a layered CO_2 plume requires fractured shale barriers within the Utsira Formation, *International Journal of Greenhouse Gas Control*, *21*, 101-112.

Chadwick, A., G. Williams, N. Delepine, V. Clochard, K. Labat, S. Sturton, M.-L. Buddensiek, M. Dillen, M. Nickel, and A. L. Lima (2010), Quantitative analysis of time-lapse seismic monitoring data at the Sleipner CO_2 storage operation, *The Leading Edge*.

Chaudhary, K., M. Bayani Cardenas, W. W. Wolfe, J. A. Maisano, R. A. Ketcham, and P. C. Bennett (2013), Pore-scale trapping of supercritical CO_2 and the role of grain wettability and shape, *Geophysical Research Letters*, *40*(15), 3878-3882.

Chaudhary, K., E. J. Guiltinan, M. B. Cardenas, J. A. Maisano, R. A. Ketcham, and P. C. Bennett (2015), Wettability measurement under high P-T conditions using X-ray imaging with application to the brine-supercritical CO_2 system, *Geochemistry, Geophysics, Geosystems*, *16*(9), 2858-2864.

Chen, S., and G. D. Doolen (1998), Lattice Boltzmann method for fluid flows, *Annu. Rev. Fluid Mech.*, *30*(1), 329-364.

Chiquet, P., D. Broseta, and S. Thibeau (2007), Wettability alteration of caprock minerals by carbon dioxide, *Geofluids*, *7*(2), 112-122.

Comisky, J. T., M. Santiago, B. McCollom, A. Buddhala, and K. E. Newsham (2011), Sample Size Effects on the Application of Mercury Injection Capillary Pressure for Determining the Storage Capacity of Tight Gas and Oil Shales, edited, Society of Petroleum Engineers.

Coon, E. T., M. L. Porter, and Q. Kang (2014), Taxila LBM: a parallel, modular lattice Boltzmann framework for simulating pore-scale flow in porous media, *Comput. Geosci.*, *18*(1), 17-27.

Crawford, B., D. Faulkner, and E. Rutter (2008), Strength, porosity, and permeability development during hydrostatic and shear loading of synthetic quartz-clay fault gouge, *Journal of Geophysical Research: Solid Earth*, *113*(B3).

Culligan, K. A., D. Wildenschild, B. S. B. Christensen, W. G. Gray, and M. L. Rivers (2006), Pore-scale characteristics of multiphase flow in porous media: A comparison of air-water and oil-water experiments, *Advances in Water Resources*, *29*(2), 227-238.

Curtis, M. E., R. J. Ambrose, C. H. Sondergeld, and C. S. Rai (2011), Transmission and Scanning Electron Microscopy Investigation of Pore Connectivity of Gas Shales on the Nanoscale, edited, Society of Petroleum Engineers.

Daigle, H. (2016), Application of critical path analysis for permeability prediction in natural porous media, *Advances in Water Resources*, *96*(Supplement C), 43-54.

Day-Stirrat, R. J., A. M. Schleicher, J. Schneider, P. B. Flemings, J. T. Germaine, and B. A. van der Pluijm (2011), Preferred orientation of phyllosilicates: Effects of composition and stress on resedimented mudstone microfabrics, *Journal of Structural Geology*, *33*(9), 1347-1358.

Dewhurst, D. N., A. C. Aplin, and J.-P. Sarda (1999), Influence of clay fraction on pore-scale properties and hydraulic conductivity of experimentally compacted mudstones, *Journal of Geophysical Research: Solid Earth*, *104*(B12), 29261-29274.

Dewhurst, D. N., A. C. Aplin, J.-P. Sarda, and Y. Yang (1998), Compaction-driven evolution of porosity and permeability in natural mudstones: An experimental study, *Journal of Geophysical Research: Solid Earth*, *103*(B1), 651-661.

DiCarlo, D. A., S. Akshay, and M. J. Blunt (2000), Three-Phase Relative Permeability of Water-Wet, Oil-Wet, and Mixed-Wet Sandpacks.

Dou, Z., Z. Zhou, and B. E. Sleep (2013), Influence of wettability on interfacial area during immiscible liquid invasion into a 3D self-affine rough fracture: Lattice Boltzmann simulations, *Advances in Water Resources*, *61*, 1-11.

Downey, M. W. (1984), Evaluating seals for hydrocarbon accumulations, *AAPG Bulletin*, *68*(11), 1752.

Edenhofer, O., R. Pichs-Madruga, Y. Sokona, E. Farahani, S. Kadner, K. Seyboth, A. Adler, I. Baum, S. Brunner, and P. Eickemeier (2014), IPCC, 2014: summary for policymakers, *Climate change*.

EIA, U. (2017), International energy outlook, *US Energy Information Administration, Washington, DC*.

Eker, E., and S. Akin (2006), Lattice Boltzmann Simulation of Fluid Flow in Synthetic Fractures, *Transport in Porous Media*, *65*(3), 363-384.

Espinoza, D. N. (2011), Carbon geological storage — Underlying phenomena and implications, ProQuest Dissertations Publishing.

Espinoza, D. N., and J. C. Santamarina (2010), Water-CO_2-mineral systems: Interfacial tension, contact angle, and diffusion-Implications to CO_2 geological storage, *Water Resources Research*, *46*.

Espinoza, D. N., and J. C. Santamarina (2017), CO_2 breakthrough-Caprock sealing efficiency and integrity for carbon geological storage, *International Journal of Greenhouse Gas Control*, *66*(Supplement C), 218-229.

Farokhpoor, R., B. J. A. Bjørkvik, E. Lindeberg, and O. Torsæter (2013), Wettability behaviour of CO_2 at storage conditions, *International Journal of Greenhouse Gas Control*, *12*(0), 18-25.

Gale, J. F. W., R. M. Reed, and J. Holder (2007), Natural fractures in the Barnett Shale and their importance for hydraulic fracture treatments, *AAPG Bulletin*, *91*(4), 603-622.

Gerke, K. M., M. V. Karsanina, and D. Mallants (2015), Universal Stochastic Multiscale Image Fusion: An Example Application for Shale Rock, *Scientific Reports*, *5*, 15880.

Germaine, J. T., and A. V. Germaine (2009), Incremental Consolidation by Oedometer, in *Geotechnical Laboratory Measurements for Engineers*, edited, pp. 294-333, John Wiley & Sons, Inc.

Grathoff, G. H., M. Peltz, F. Enzmann, and S. Kaufhold (2016), Porosity and permeability determination of organic-rich Posidonia shales based on 3-D analyses by FIB-SEM microscopy, *SOLID EARTH, 7*(4), 1145-1156.

Guiltinan, E. J., M. B. Cardenas, P. C. Bennett, T. Zhang, and D. N. Espinoza (2017), The effect of organic matter and thermal maturity on the wettability of supercritical CO_2 on organic shales, *International Journal of Greenhouse Gas Control, 65*(Supplement C), 15-22.

Han, W. S., B. J. McPherson, P. C. Lichtner, and F. P. Wang (2010), Evaluation of trapping mechanisms in geologic CO_2 sequestration: Case study of SACROC northern platform, a 35-year CO_2 injection site, *American Journal of Science, 310*(4), 282-324.

Hao, L., and P. Cheng (2010), Pore-scale simulations on relative permeabilities of porous media by lattice Boltzmann method, *International Journal of Heat and Mass Transfer, 53*(9-10), 1908-1913.

Harrington, J., D. Noy, S. Horseman, D. Birchall, and R. Chadwick (2009), Laboratory study of gas and water flow in the Nordland Shale, Sleipner, North Sea.

Hartmann, D. J., and E. A. Beaumont (1999), Treatise of Petroleum Geology/Handbook of Petroleum Geology: Exploring for Oil and Gas Traps. Chapter 9: Predicting Reservoir System Quality and Performance.

Hildenbrand, A., S. Schlömer, and B. M. Krooss (2002), Gas breakthrough experiments on fine-grained sedimentary rocks, *Geofluids, 2*(1), 3-23.

Hildenbrand, A., S. Schlömer, B. M. Krooss, and R. Littke (2004), Gas breakthrough experiments on pelitic rocks: comparative study with N2, CO_2 and CH4, *Geofluids, 4*(1), 61-80.

Hu, Q., X. Gao, Z. Gao, R. Ewing, S. Dultz, and J. Kaufmann (2014), Pore Accessibility and Connectivity of Mineral and Kerogen Phases in Shales, edited, Unconventional Resources Technology Conference.

Hu, R., J. Wan, Y. Kim, and T. K. Tokunaga (2017), Wettability effects on supercritical CO_2–brine immiscible displacement during drainage: Pore-scale observation and 3D simulation, *International Journal of Greenhouse Gas Control, 60*, 129-139.

Hu, Y. A., D. Devegowda, and R. Sigal (2016), A microscopic characterization of wettability in shale kerogen with varying maturity levels, *Journal of Natural Gas Science and Engineering, 33*(Journal Article), 1078-1086.

IEA (2017), Global EV Outlook 2017, *International Energy Agency*.

Iglauer, S., C. H. Pentland, and A. Busch (2015), CO_2 wettability of seal and reservoir rocks and the implications for carbon geo-sequestration, *Water Resources Research*, *51*(1), 729-774.

Iglauer, S., A. Z. Al-Yaseri, R. Rezaee, and M. Lebedev (2015), CO_2 wettability of caprocks: Implications for structural storage capacity and containment security, *Geophysical Research Letters*, *42*(21), 9279-9284.

Iglauer, S., A. Salamah, M. Sarmadivaleh, K. Liu, and C. Phan (2014), Contamination of silica surfaces: Impact on water–CO_2–quartz and glass contact angle measurements, *International Journal of Greenhouse Gas Control*, *22*(0), 325-328.

Ilgen, A. G., J. E. Heath, I. Y. Akkutlu, L. T. Bryndzia, D. R. Cole, Y. K. Kharaka, T. J. Kneafsey, K. L. Milliken, L. J. Pyrak-Nolte, and R. Suarez-Rivera (2017), Shales at all scales: Exploring coupled processes in mudrocks, *Earth-Science Reviews*, *166*, 132-152.

IPCC (2005), Underground geological storage*Rep.*, 195-276 pp.

Jarvie, D. M., R. J. Hill, T. E. Ruble, and R. M. Pollastro (2007), Unconventional shale-gas systems: The Mississippian Barnett Shale of north-central Texas as one model for thermogenic shale-gas assessment, *AAPG Bulletin*, *91*(4), 475-499.

Ju, Y., Q. Zhang, J. Zheng, C. Chang, and H. Xie (2017), Fractal model and Lattice Boltzmann Method for Characterization of Non-Darcy Flow in Rough Fractures, *Scientific Reports*, *7*, 41380.

Juanes, R., E. J. Spiteri, F. M. Orr, and M. J. Blunt (2006), Impact of relative permeability hysteresis on geological CO_2 storage, *Water Resources Research*, *42*(12), 13.

Jung, J.-W., and J. Wan (2012), Supercritical CO_2 and Ionic Strength Effects on Wettability of Silica Surfaces: Equilibrium Contact Angle Measurements, *Energy & Fuels*, *26*(9), 6053-6059.

Jung, J. W., J. Jang, J. C. Santamarina, C. Tsouris, T. J. Phelps, and C. J. Rawn (2012), Gas Production from Hydrate-Bearing Sediments: The Role of Fine Particles, *Energy & Fuels*, *26*(1), 480-487.

Kampman, N., N. M. Burnside, Z. K. Shipton, H. J. Chapman, J. A. Nicholl, R. M. Ellam, and M. J. Bickle (2012), Pulses of carbon dioxide emissions from intracrustal faults following climatic warming, *NATURE GEOSCIENCE*, *5*(5), 352-358.

Katz, A. J., and A. H. Thompson (1987), Prediction of rock electrical conductivity from mercury injection measurements, *Journal of Geophysical Research: Solid Earth*, *92*(B1), 599-607.

Kianinejad, A., X. Chen, and D. A. DiCarlo (2016), Direct measurement of relative permeability in rocks from unsteady-state saturation profiles, *Advances in Water Resources*, *94*, 1-10.

Kim, I., W. Lindquist, and W. Durham (2003), Fracture flow simulation using a finite-difference lattice Boltzmann method, *Physical Review E*, *67*(4), 046708

King, D., J. Browne, R. Layard, G. O'Donnell, M. Rees, N. Stern, and A. Turner (2015), A global Apollo programme to combat climate change, *Centre for Economic Performance, London School of Economics and Political Science. http://cep. lse. ac. uk/pubs/download/special/Global_Apollo_Programme_Report. pdf [accessed 9 October 2015]*.

Kinley, T. J., L. W. Cook, J. A. Breyer, D. M. Jarvie, and A. B. Busbey (2008), Hydrocarbon potential of the Barnett Shale (Mississippian), Delaware Basin, west Texas and southeastern New Mexico, *AAPG Bulletin*, *92*(8), 967-991.

Lan, Q., M. Xu, M. Binazadeh, H. Dehghanpour, and J. M. Wood (2015), A comparative investigation of shale wettability: The significance of pore connectivity, *Journal of Natural Gas Science and Engineering*, *27, Part 2*, 1174-1188.

Landry, C. J., Z. T. Karpyn, and O. Ayala (2014a), Pore-Scale Lattice Boltzmann Modeling and 4D X-ray Computed Microtomography Imaging of Fracture-Matrix Fluid Transfer, *Transport in Porous Media*, *103*(3), 449-468.

Landry, C. J., Z. T. Karpyn, and O. Ayala (2014b), Relative permeability of homogenous-wet and mixed-wet porous media as determined by pore-scale lattice Boltzmann modeling, *Water Resources Research*, *50*(5), 3672-3689.

Laplace, P. S., N. Bowditch, and N. I. Bowditch (1829), Mécanique céleste, *Meccanica*, *1*.

Larson, R. G., L. E. Scriven, and H. T. Davis (1981), Percolation theory of two phase flow in porous media, *Chemical Engineering Science*, *36*(1), 57-73.

Li, S., M. Dong, Z. Li, S. Huang, H. Qing, and E. Nickel (2005), Gas breakthrough pressure for hydrocarbon reservoir seal rocks: implications for the security of long-term CO_2 storage in the Weyburn field, *Geofluids*, *5*(4), 326-334.

Loucks, R. G., and S. C. Ruppel (2007), Mississippian Barnett Shale: Lithofacies and depositional setting of a deep-water shale-gas succession in the Fort Worth Basin, Texas, *AAPG Bulletin*, *91*(4), 579-601.

Loucks, R. G., R. M. Reed, S. C. Ruppel, and D. M. Jarvie (2009), Morphology, Genesis, and Distribution of Nanometer-Scale Pores in Siliceous Mudstones of the Mississippian Barnett Shale, *Journal of Sedimentary Research*, *79*(12), 848-861.

Lucena, L., J. Freitas, G. Corso, and R. Soares (2003), Anisotropy and percolation threshold in a multifractal support, *Brazilian Journal of Physics*, *33*(3), 637-640.

Makhnenko, R. Y., V. Vilarrasa, D. Mylnikov, and L. Laloui (2017), Hydromechanical Aspects of CO_2 Breakthrough into Clay-rich Caprock, *Energy Procedia*, *114*(Supplement C), 3219-3228.

Masihi, M., P. R. King, and P. Nurafza (2006), Effect of anisotropy on finite-size scaling in percolation theory, *Physical Review E*, *74*(4), 042102.

Milliken, K. L., M. Rudnicki, D. N. Awwiller, and T. W. Zhang (2013), Organic matter-hosted pore system, Marcellus Formation (Devonian), Pennsylvania, *AAPG Bulletin*, *97*(2), 177-200.

Mills, J., M. Riazi, and M. Sohrabi (2011), Wettability of common rock-forming minerals in a CO_2-brine system at reservoir conditions, paper presented at International Symposium of the Society of Core Analysts, Texas, USA.

Mondol, N. H., K. Bjørlykke, J. Jahren, and K. Høeg (2007), Experimental mechanical compaction of clay mineral aggregates—Changes in physical properties of mudstones during burial, *Marine and Petroleum Geology*, *24*(5), 289-311.

Mondol, N. H., M. Fawad, J. Jahren, and K. Bjorlykke (2008), Synthetic mudstone compaction trends and their use in pore pressure prediction, *first break*, *26*(12), 43-51.

Montgomery, S. L., D. M. Jarvie, K. A. Bowker, and R. M. Pollastro (2005), Mississippian Barnett Shale, Fort Worth basin, north-central Texas: Gas-shale play with multi-trillion cubic foot potential, *AAPG Bulletin*, *89*(2), 155-175.

Nelson, P. H. (2009), Pore-throat sizes in sandstones, tight sandstones, and shales, *AAPG Bulletin*, *93*(3), 329-340.

Nordbotten, J. M., M. A. Celia, and S. Bachu (2005), Injection and Storage of CO_2 in Deep Saline Aquifers: Analytical Solution for CO_2 Plume Evolution During Injection, *Transport in Porous Media*, *58*(3), 339-360.

Nourgaliev, R. R., T. N. Dinh, T. G. Theofanous, and D. Joseph (2003), The lattice Boltzmann equation method: theoretical interpretation, numerics and implications, *International Journal of Multiphase Flow*, *29*(1), 117-169.

Ogilvie, S. R., E. Isakov, and P. W. J. Glover (2006), Fluid flow through rough fractures in rocks. II: A new matching model for rough rock fractures, *Earth and Planetary Science Letters*, *241*(3), 454-465.

Peng, S., T. Zhang, R. G. Loucks, and J. Shultz (2017), Application of mercury injection capillary pressure to mudrocks: Conformance and compression corrections, *Marine and Petroleum Geology*, *88*(Supplement C), 30-40.

Penumadu, D., and J. Dean (2000), Compressibility effect in evaluating the pore-size distribution of kaolin clay using mercury intrusion porosimetry, *Canadian Geotechnical Journal*, *37*(2), 393-405.

Peters, E. J. (2012), *Advanced Petrophysics: Dispersion, interfacial phenomena*, Greenleaf Book Group.

Petroff, A. (2017), These Countries Want to Ban Gas And Diesel Cars, *CNN, Accessed at http://money.cnn.com/2017/09/11/autos/countries-banning-diesel-gas-cars/index.html*.

Porter, M. L., E. T. Coon, Q. Kang, J. D. Moulton, and J. W. Carey (2012), Multicomponent interparticle-potential lattice Boltzmann model for fluids with large viscosity ratios, *Physical Review E*, *86*(3), 036701.

Purcell, W. R. (1949), Capillary Pressures - Their Measurement Using Mercury and the Calculation of Permeability Therefrom.

Ramstad, T., N. Idowu, C. Nardi, and P.-E. Øren (2012), Relative Permeability Calculations from Two-Phase Flow Simulations Directly on Digital Images of Porous Rocks, *Transport in Porous Media*, *94*(2), 487-504.

Reece, J., P. Flemings, and J. Germaine (2013), Data report: Permeability, compressibility, and microstructure of resedimented mudstone from IODP Expedition 322, Site C0011, paper presented at Proceedings of the Integrated Ocean Drilling Program.

Renshaw, C. E. (1995), On the relationship between mechanical and hydraulic apertures in rough-walled fractures, *Journal of Geophysical Research: Solid Earth*, *100*(B12), 24629-24636.

Rohmer, J., A. Pluymakers, and F. Renard (2016), Mechano-chemical interactions in sedimentary rocks in the context of CO_2 storage: Weak acid, weak effects?, *Earth-Science Reviews*, *157*, 86-110.

Romero-Sarmiento, M.-F., J.-N. Rouzaud, S. Bernard, D. Deldicque, M. Thomas, and R. Littke (2014), Evolution of Barnett Shale organic carbon structure and nanostructure with increasing maturation, *Organic Geochemistry*, *71*, 7-16.

Roshan, H., A. Z. Al-Yaseri, M. Sarmadivaleh, and S. Iglauer (2016), On wettability of shale rocks, *Journal of Colloid and Interface Science*, *475*(Journal Article), 104-111.

Rubin, E. S., J. E. Davison, and H. J. Herzog (2015), The cost of CO_2 capture and storage, *International Journal of Greenhouse Gas Control*, *40*, 378-400.

Sadeghnejad, S., M. Masihi, P. R. King, A. Shojaei, and M. Pishvaei (2010), Effect of anisotropy on the scaling of connectivity and conductivity in continuum percolation theory, *Physical Review E*, *81*(6), 061119.

Saraji, S., L. Goual, M. Piri, and H. Plancher (2013), Wettability of Supercritical Carbon Dioxide/Water/Quartz Systems: Simultaneous Measurement of Contact Angle and Interfacial Tension at Reservoir Conditions, *Langmuir*, *29*(23), 6856-6866.

Sarmadivaleh, M., A. Z. Al-Yaseri, and S. Iglauer (2015), Influence of temperature and pressure on quartz–water–CO_2 contact angle and CO_2–water interfacial tension, *Journal of Colloid and Interface Science*, *441*, 59-64.

Schneider, J., P. B. Flemings, R. J. Day-Stirrat, and J. T. Germaine (2011), Insights into pore-scale controls on mudstone permeability through resedimentation experiments, *Geology*, *39*(11), 1011-1014.

Schowalter, T. T. (1979), Mechanics of secondary hydrocarbon migration and entrapment, *AAPG Bulletin*, *63*(5), 723-760.

Shafiee, A. (2008), Permeability of compacted granule–clay mixtures, *Engineering Geology*, *97*(3), 199-208.

Shan, X. (2006), Analysis and reduction of the spurious current in a class of multiphase lattice Boltzmann models, *Physical Review E*, *73*(4), 047701.

Shan, X., and H. Chen (1993), Lattice Boltzmann model for simulating flows with multiple phases and components, *Physical Review E*, *47*(3), 1815-1819.

Shan, X., and H. Chen (1994), Simulation of nonideal gases and liquid-gas phase transitions by the lattice Boltzmann equation, *Physical Review E*, *49*(4), 2941-2948.

Sherwood, P. (1993), *Soil stabilization with cement and lime*.

Shin, H., and J. C. Santamarina (2011), Desiccation cracks in saturated fine-grained soils: particle-level phenomena and effective-stress analysis, *Géotechnique*, *61*(11), 961-972.

Shojai Kaveh, N., A. Barnhoorn, and K. H. Wolf (2016), Wettability evaluation of silty shale caprocks for CO_2 storage, *International Journal of Greenhouse Gas Control*, *49*(Journal Article), 425-435.

Skurtveit, E., E. Aker, M. Soldal, M. Angeli, and Z. Wang (2012), Experimental investigation of CO_2 breakthrough and flow mechanisms in shale, *Petroleum Geoscienc*, *18*(1), 3-15.

Šolc, R., M. H. Gerzabek, H. Lischka, and D. Tunega (2011), Wettability of kaolinite (001) surfaces — Molecular dynamic study, *Geoderma*, *169*(Supplement C), 47-54.

Sondergeld, C. H., R. J. Ambrose, C. S. Rai, and J. Moncrieff Micro-Structural Studies of Gas Shales, edited, Society of Petroleum Engineers.

Tenney, C. M., T. Dewers, K. Chaudhary, E. N. Matteo, M. B. Cardenas, and R. T. Cygan (2017), Experimental and simulation study of carbon dioxide, brine, and muscovite surface interactions, *Journal of Petroleum Science and Engineering*, *155*, 78-88.

Terzaghi, K., and R. B. Peck (1948), *Soil mechanics in engineering practice*, J. Wiley, New York US

Tokunaga, T. K., J. M. Wan, J. W. Jung, T. W. Kim, Y. Kim, and W. M. Dong (2013), Capillary pressure and saturation relations for supercritical CO_2 and brine in sand: High-pressure P-c(S-w) controller/meter measurements and capillary scaling predictions, *Water Resources Research*, *49*(8), 4566-4579.

Trevisan, L., P. G. Krishnamurthy, and T. A. Meckel (2017), Impact of 3D capillary heterogeneity and bedform architecture at the sub-meter scale on CO_2 saturation for buoyant flow in clastic aquifers, *International Journal of Greenhouse Gas Control*, *56*(Supplement C), 237-249.

Vogler, D., R. R. Settgast, C. Annavarapu, C. Madonna, P. Bayer, and F. Amann (2018), Experiments and Simulations of Fully Hydro-Mechanically Coupled Response of Rough Fractures Exposed to High-Pressure Fluid Injection, *Journal of Geophysical Research: Solid Earth*, *123*(2), 1186-1200.

Wang, L., and M. B. Cardenas (2014), Non-Fickian transport through two-dimensional rough fractures: Assessment and prediction, *Water Resources Research*, *50*(2), 871-884.

Wang, L., M. B. Cardenas, D. T. Slottke, R. A. Ketcham, and J. M. Sharp (2015), Modification of the Local Cubic Law of fracture flow for weak inertia, tortuosity, and roughness, *Water Resources Research*, *51*(4), 2064-2080.

Wang, S., Z. Tao, S. M. Persily, and A. F. Clarens (2013), CO_2 Adhesion on Hydrated Mineral Surfaces, *Environ. Sci. Technol.*, *47*(20), 11858-11865.

Wollenweber, J., S. Alles, A. Busch, B. Kroos, H. Stanjek, and R. Littke (2010), Experimental investigation of the CO 2 sealing efficiency of caprocks, *International Journal of Greenhouse Gas Control*, *4*(2), 231-241.

Yang, Y., and A. C. Aplin (2010), A permeability–porosity relationship for mudstones, *Marine and Petroleum Geology*, *27*(8), 1692-1697.

Young, T. (1805), An Essay on the Cohesion of Fluids, *Philosophical Transactions of the Royal Society of London*, *95*, 65-87.

Yu, Z., H. Yang, and L.-S. Fan (2011), Numerical simulation of bubble interactions using an adaptive lattice Boltzmann method, *Chemical Engineering Science*, *66*(14), 3441-3451.

Zhang, J. (2011), Lattice Boltzmann method for microfluidics: models and applications, *Microfluidics and Nanofluidics*, *10*(1), 1-28.

Zhang, T., G. S. Ellis, S. C. Ruppel, K. Milliken, and R. Yang (2012), Effect of organic-matter type and thermal maturity on methane adsorption in shale-gas systems, *Organic Geochemistry*, *47*, 120-131.

Zhang, T., R. Yang, K. L. Milliken, S. C. Ruppel, R. J. Pottorf, and X. Sun (2014), Chemical and isotopic composition of gases released by crush methods from organic rich mudrocks, *Organic Geochemistry*, *73*, 16-28.

Zhao, J., Q. Kang, J. Yao, H. Viswanathan, R. Pawar, L. Zhang, and H. Sun (2018), The Effect of Wettability Heterogeneity on Relative Permeability of Two-Phase Flow in Porous Media: A Lattice Boltzmann Study, *Water Resources Research*, *54*(2), 1295-1311.